

COPYRIGHT WARNING

This paper is protected by copyright. You are advised to print or download **ONE COPY** of this paper for your own private reference, study and research purposes. You are prohibited having acts infringing upon copyright as stipulated in Laws and Regulations of Intellectual Property, including, but not limited to, appropriating, impersonating, publishing, distributing, modifying, altering, mutilating, distorting, reproducing, duplicating, displaying, communicating, disseminating, making derivative work, commercializing and converting to other forms the paper and/or any part of the paper. The acts could be done in actual life and/or via communication networks and by digital means without permission of copyright holders.

The users shall acknowledge and strictly respect to the copyright. The recitation must be reasonable and properly. If the users do not agree to all of these terms, do not use this paper. The users shall be responsible for legal issues if they make any copyright infringements. Failure to comply with this warning may expose you to:

- Disciplinary action by the Vietnamese-German University.
- Legal action for copyright infringement.
- Heavy legal penalties and consequences shall be applied by the competent authorities.

The Vietnamese-German University and the authors reserve all their intellectual property rights.





RUHR-UNIVERSITÄT BOCHUM

MechEng
Mechanical Engineering



Vietnamese-German University

MOLECULAR DYNAMICS SIMULATION STUDY ON SEPARATION OF DIAMONDOIDS IN OILS USING NANOPOROUS MATERIALS

BACHELOR THESIS

BINH DUONG, MAY 2023



Vietnamese-German University

Submitted by: Nguyen Minh Trung

RUB Student ID: 19220800

VGU Student ID: 14318

Supervisor: Dr. Nguyen Xuan Thanh

The Bachelor Thesis of Nguyen Minh Trung, titled *MOLECULAR DYNAMICS SIMULATION STUDY ON SEPARATION OF DIAMONDOIDS IN OILS USING NANOPOROUS MATERIALS*, is approved by:

Supervisor: Dr. Nguyen Xuan Thanh, Senior Lecturer of Mechanical Engineering Program, Vietnamese-German University, Binh Duong Province, Vietnam

Signature: _____



© by Nguyen Minh Trung, May, 2023
All Rights Reserved

I hereby declare that this document is my own work and that it does not contain other people's work without this being so stated; this thesis does not contain any of my previous work without this being stated, and the bibliography contains all the literature used in writing the dissertation.

I declare that this is a true copy of my thesis, including any final revisions, as approved by my supervisor, and that this thesis has not been submitted for a higher degree to any other university or institution.

I certify that any republication of materials presented in this thesis has been approved by the relevant publishers and co-authors.

Signature:  _____
Nguyen Minh Trung
May, 2023

Acknowledgements

It is important to show great appreciation from the author for the supervision and support of Dr. Nguyen Xuan Thanh so as to complete the project with greater accomplishment than expected.



Abstract

Diamondoids are cage-like structures having from one to a few unit cells of the diamond structure and so-called nanodiamond-sized molecules. Hence, the diamondoids have rigidity and excellent thermal stability resembling the bulk diamond. Diamondoids have been found in traceable amounts in extractable organic matter (EOM) from source rocks and moderate maturity oils and high concentrations in condensates as well as highly matured crude oils due to their higher thermal stability than the non-diamondoids. Despite the abiogenic origin of the diamondoids, stable carbon isotope ratios ($^{13}\text{C}/^{12}\text{C}$) of diamondoids have been shown as a proxy tool to evaluate oil-oil and oil-source correlations, especially for highly matured oils and condensates in which biomarkers such as hopanes and steranes are mostly absent due to thermal degradation over geological time. Nevertheless, the measurement of stable carbon isotope ratios of diamondoids by gas chromatography isotope ratio mass spectrometer (GCIRMS) essentially requires the gas chromatographic separation of these compounds from oils and EOM. Furthermore, despite the diamond-like structure, diamondoids have distinct optoelectronic properties including negative electron affinity (NEA) for flat panel field-emission displays, and the tunability of the direct band gap energy in ultraviolet (UV) wavelength. These interesting optoelectronic properties result from the hydrogen-terminated surface and size of diamondoids. Despite the numerous methods developed to synthesize diamondoids, they are generally not efficient and the underlying mechanism to form diamondoids is not well understood. Therefore, the separation of diamondoids from petroleum is highly regarded. In our previous work, adamantane and its derivatives are successfully separated from oils by the heat-treated version of commercial β -zeolite. However, the underlying separation mechanism by adsorption has not been elucidated. As a result, in this thesis, the mechanism of the separation of the diamondoids from oil by adsorption at the nanoscale is investigated using molecular dynamics (MD) simulation. Accordingly, we have found that there is molecular sieving to exclude diamondoids by the virgin β -zeolite model, revealing the heat treatment of the β -zeolite leads to the lateral pore opening that enhances the adsorption of larger cyclic alkanes while still excluding diamondoids. This is in good agreement with the previous experimental observation. Furthermore, the adsorption dynamics studies of adamantane, benzene, and 2,2-dimethyl hexane in activated carbon ACF-15 and graphitic slit-like pore models show that there is the molecular sieving to exclude adamantane from the graphitic pore of 5.5 Å while the predominant adsorption of adamantane over benzene and 2,2-dimethyl hexane has been observed for the graphitic pore of 12 Å due to the stability of molecular self-assembly of the adsorbed adamantane phase in this pore. At the same time, only slightly preferential adsorption of adamantane over benzene and 2,2-dimethyl hexane has been observed in the disordered porous carbon-like activated carbon fiber ACF-15.

Table of Contents

Acknowledgements	iv
Abstract	v
Table of Contents	vi
List of Figures	vi
1 Introduction	1
2 Methodologies and materials	8
2.1 Molecular dynamics simulation principle	8
2.2 Force field	9
2.3 Molecular dynamics analysis	11
2.4 Materials	14
3 Results and discussion	21
3.1 Adsorption dynamics in β -zeolite	21
3.2 Adsorption dynamics of Hydrocarbons in Realistic Structural Model of Activated Carbon Fiber ACF-15	25
3.3 Adsorption dynamics of Hydrocarbons in Graphitic Slit-Like Pore	33
4 Conclusions	42
5 References	44
A Mean square displacement	48
B Velocity autocorrelation function	49
C Radial distribution function	50



List of Figures

1.1	An illustration of carbon nanostructures generated as a result of various hybridizations of C, sp^1 , sp^2 , and sp^3	2
1.2	Structures of lower and higher diamondoids particle	2
1.3	Schematic of adamantane synthesis	3
1.4	Process flow diagram of electric discharge in SCFs to synthesize diamondoids	4
1.5	Side view of the high-pressure cell	5
1.6	(a) Three-dimension of a micro-reactors. (b) Cross area of a single micro-reactor channel.	5
1.7	Schematic two-segment column for diamondoid separation	6
1.8	GC trace of adamantane and methylated derivatives separated from sample OM1 using two-segment column (HT-CP814 E°)	7
2.1	Bond distances and angles in intramolecular potentials	10
2.2	Coarse-grained potential illustration. (a) A methyl group ($-CH_3$) is simplified as a single point of interaction. (b) A united-atom potential of the atoms in a small chain.	11
2.3	(a) Structure of a close-packed fcc lattice computed for 108 atoms and periodic boundary conditions. (b) Structure of a close-packed simple cubic lattice computed for 125 atoms and periodic boundary conditions.	13
2.4	Radial distribution function for gas and liquid phases of the Lennard-Jones fluid	14
2.5	Unit cell and construction of graphene model	15
2.6	Configuration of graphitic slit-pore model	15
2.7	Snapshot of ACF-15	16
2.8	Structure of β -zeolite. (a) The unit cell of beta polymorph A. (b) Supercell of β -zeolite.	16
2.9	Structure of lower diamondoids	17
2.10	Structure of 22DMC6	19
2.11	Structure of benzene	20
3.1	Investigation on adsorption accessibility of the synthetic oil to β -zeolite adsorbent. (a) MD initial configuration of the synthetic oil in β -zeolite. (b) MD initial configuration does not contain the synthetic oil in β -zeolite. (c) MD snapshot of the hydrocarbons inside β -zeolite after 3ns run.	21
3.2	Investigation on adsorption accessibility of pure hydrocarbon to β -zeolite adsorbent. (c) MD Initial configuration of alkane in β -zeolite. (d) MD snapshot of alkane in β -zeolite. (e) MD Initial configuration of benzene in β -zeolite. (f) MD snapshot of benzene in β -zeolite.	22
3.3	Adsorbtion dynamics analysis in β -zeolite. (a) Self-diffusivity of pure hydrocarbons in β -Zeolite at 298 K. (b) Time-dependent MSD of pure hydrocarbons in β -Zeolite at 298 K.	24
3.4	Investigation on adsorption accessibility of adamantane to ACF-15. (a) MD initial configuration of adamantane in ACF-15. (b) The configuration of adamantane in ACF-15 after 3ns MD run before taking out the solid. (c) The configuration of adamantane in ACF-15 after 3ns MD run after taking out the solid.	26
3.5	Time-dependent MSD of adamantane in ACF-15 at various temperatures.	26

3.6	Adsorption dynamics analysis of adamantane in ACF-15. (a) Self-diffusivity of adamantane in ACF-15 at various temperatures. (b) Arrhenius fitting of self-diffusivity of adamantane in ACF-15 against temperatures.	28
3.7	Radial distribution function of adamantane in ACF-15 at various temperatures.	29
3.8	Investigation on adsorption accessibility of pure hydrocarbons to ACF-15 adsorbent. (a) MD Initial configuration of alkane in ACF-15. (b) MD snapshot of alkane in ACF-15. (c) MD Initial configuration of benzene in ACF-15. (d) MD snapshot of benzene in ACF-15.	30
3.9	Self-diffusivity of pure hydrocarbons in ACF-15 at 298 K.	31
3.10	Investigation on adsorption accessibility of synthetic oil to ACF-15. (a) MD initial configuration of synthetic oil in ACF-15. (b) The configuration of synthetic oil in ACF-15 after 3ns MD run before taking out the solid. (c) The configuration of synthetic oil in ACF-15 after 3ns MD run after taking out the solid.	31
3.11	Radial distribution function of adamantane in synthetic oil in ACF-15 at various temperatures.	32
3.12	Adsorption dynamics analysis of adamantane in ACF-15. (a) Self-diffusivity of hydrocarbons of synthetic oil in ACF-15 at various temperatures. (b) Self-diffusivity of hydrocarbons of synthetic oil in ACF-15 against temperatures.	32
3.13	Investigation on adsorption accessibility of adamantane to 5.5 Å graphitic slit pore. (a) MD initial configuration of adamantane in graphitic slit pore. (b) The configuration of adamantane in graphitic slit pore after 3ns MD run. (c) MD initial configuration has no adamantane in graphitic slit pore after 3ns MD run.	33
3.14	Investigation on adsorption accessibility of benzene to 5.5 Å graphitic slit pore. (a) MD initial configuration of benzene in graphitic slit pore. (b) The configuration of benzene in graphitic slit pore after 3ns MD run. (c) The configuration of benzene in graphitic slit pore of 3ns MD run after taking out the solid.	33
3.15	Investigation on adsorption accessibility of alkane to 5.5 Å graphitic slit pore. (a) MD initial configuration of alkane in graphitic slit pore. (b) The configuration of alkane in graphitic slit pore after 3ns MD run. (c) The configuration of alkane in graphitic slit pore of 3ns MD run after taking out the solid.	34
3.16	Investigation on adsorption accessibility of the synthetic oil to 5.5 Å graphitic slit pore. (a) MD initial configuration of the synthetic oil in 5.5 Å graphitic slit pore. (b) MD snapshot indicates molecular sieving excluding adamantane from the pore size of 5.5 Å.	36
3.17	Investigation on adsorption accessibility of the synthetic oil to 6 Å graphitic slit pore. (a) MD initial configuration of the synthetic oil in 6 Å graphitic slit pore. (b) MD snapshot of synthetic oil in 6 Å graphitic slit pore of 3ns MD run after taking out the solid.	37
3.18	Investigation on adsorption accessibility of the synthetic oil to 9 Å graphitic slit pore. (a) MD initial configuration of the synthetic oil in 9 Å graphitic slit pore. (b) MD snapshot of synthetic oil in 9 Å graphitic slit pore of 5ns MD run after taking out the solid.	37
3.19	Investigation on adsorption accessibility of the synthetic oil to 12 Å graphitic slit pore. (a) MD initial configuration of the synthetic oil in 12 Å graphitic slit pore. (b) MD snapshot of synthetic oil in 12 Å graphitic slit pore of 5ns MD run after taking out the solid.	38

3.20	Investigation on adsorption accessibility of the synthetic oil to 15 Å graphitic slit pore. (a) MD initial configuration of the synthetic oil in 15 Å graphitic slit pore. (b) MD snapshot of synthetic oil in 15 Å graphitic slit pore of 5ns MD run after taking out the solid.	38
3.21	Molecular packing configuration in the pore size of 12 Å	38
3.22	Radial distribution function of adamantane in synthetic oil at different pore sizes	39
3.23	Adamantane adsorption dynamics analysis in graphitic slit pore at different pore sizes. (a) Self-diffusivity of hydrocarbons of synthetic oil in 6 Å graphitic slit pore. (b) Self-diffusivity of hydrocarbons of synthetic oil in 9 Å graphitic slit pore. (c) Self-diffusivity of hydrocarbons of synthetic oil in 12 Å graphitic slit pore. (d) Self-diffusivity of hydrocarbons of synthetic oil in 15 Å graphitic slit pore. . . .	39
3.24	Self-diffusivity of hydrocarbons of synthetic oil in graphitic slit pore at different pore sizes	40
3.25	Self-diffusivity of hydrocarbons of synthetic oil in 12 Å graphitic pore at different temperatures	40
3.26	Radial distribution function of adamantane in synthetic oil inside 12 Å graphitic pore at different temperatures	41



CHAPTER 1

Introduction

Carbon is one of the foremost prolific elements on earth (Atkins et al., 2010)¹, and many different nanomaterials, such as graphene, carbon nanotubes, fullerenes, and nanodiamonds can be formed as a consequence of various hybridizations. Landa and Machacek discovered diamondoids - the aliphatic cage-like hydrocarbons in petroleum in 1933, creating a new field of chemistry, especially for the synthesis and characteristics of polyhedral organic molecules (Schoell and Carlson, 1999)². The diamondoid molecules essentially contain at least one complete adamantane unit (Balaban and Schleyer, 1978)³, and their name was rooted in the similar structure of the diamond crystal lattice (it is symmetrical and there is no strain). Adamantane (C₁₀H₁₆) is a small hydrocarbon molecule with a tetrahedral point group of sp³ hybridized carbon atoms (Hernández-Rojas and Calvo, 2019)⁴.

Diamondoids have higher thermal stability compared to alkanes that have equal molecular weight, resulting in their significantly enhanced concentration in mature oils and condensates (Dahl et al., 1999)⁵. Hence, the constant growth of diamondoid concentration in oils due to higher thermal maturity can potentially be used to predict the occurrence, degree of oil devastation, and the oil deadline in a specific reservoir. Diamondoids are also used in environmental forensics and medical treatment. In particular, the corresponding abundance of various diamondoids and their derivatives, particularly adamantane and diamantane, as well as their high heat resistance, can be utilized to identify oil and gas resources in various places. Diamondoids, for instance, were exploited to analyze the maturity of gas condensates in Pakistan's Southern Indus Basin (Nasir and Fazeelat, 2013)⁶. The high resistance of diamondoids to biodegradation is useful for the identification of the source of oil spills (Mansuy et al., 1997⁷; Lengger et al., 2013⁸). More recently stable carbon isotope (¹³C/¹²C) ratios of lower diamondoids have been utilized as a reliable tool for high mature oil-oil and oil-source rock correlations. Diamondoids are also gaining popularity in other prospective applications. Because of the fluorescence brightness, methylated adamantanes were discovered to be suitable candidates for optical and electrical applications (able to customize fluorescent and electronic properties of nanomaterials) (Rander et al., 2017)⁹. Diamondoid molecules with a hydrogen-terminated surface having a Negative Electron Affinity (NEA) property facilitate the accumulation and stimulated emission of the excited electrons from the metal to the vacuum. In this regard, the NEA property of diamondoids is used to make the electron-emitting device or electron gun. In addition, the lowest unoccupied molecular orbital (LUMO) energy level varies in the size of the nano-diamondoid molecule while the highest occupied molecular orbital (HOMO) energy level is insensitive. This enables tuning the bandgap energy of diamondoids,

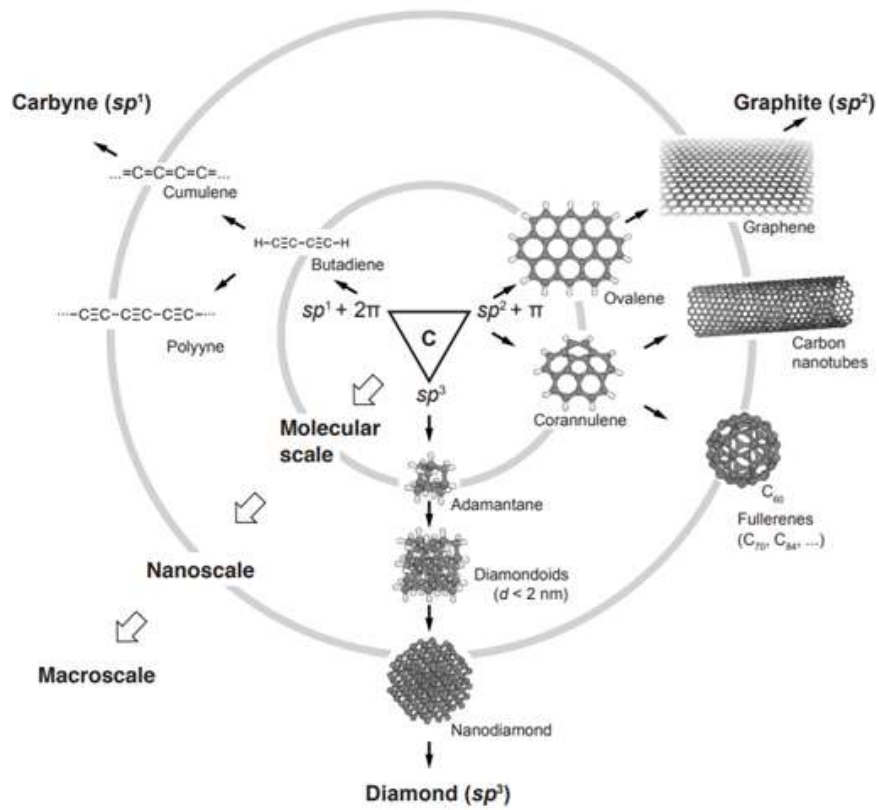


Figure 1.1: An illustration of carbon nanostructures generated as a result of various hybridizations of C, sp^1 , sp^2 , and sp^3



Vietnamese-German University

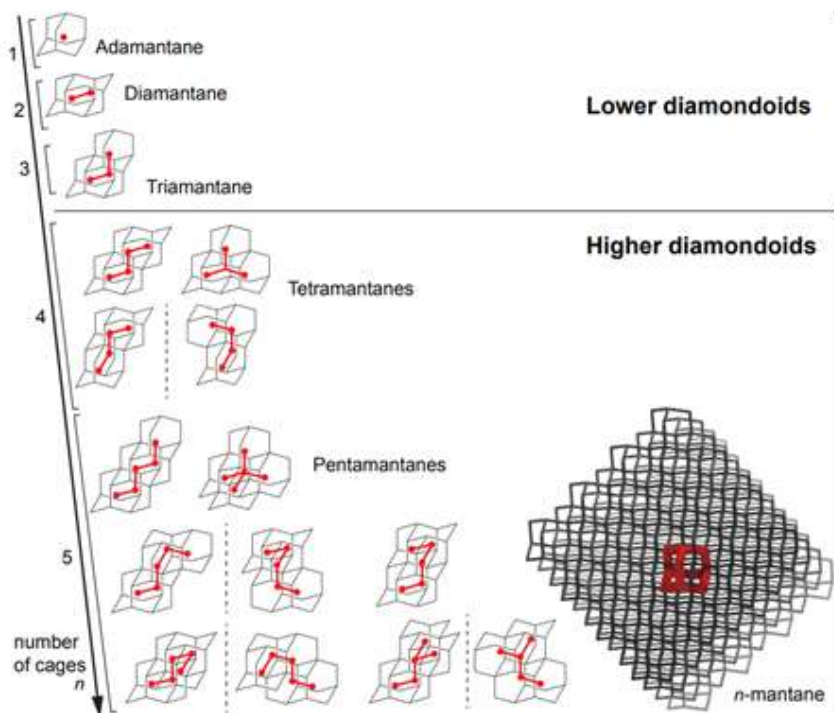


Figure 1.2: Structures of lower and higher diamondoids particle

which is one of the key optical parameters. Some alkyl adamantanes are regarded as possible diesel enhancers because of their higher density and higher cetane characteristics (Harvey et al., 2016)¹⁰. Adamantane is also used as a standard for chemical shift reference in solid-state NMR spectroscopy (Morcombe et al., 2003)¹¹. Adamantane derivatives are employed in medical applications due to their non-toxicity. Amantadine, for example, is an antiviral medicine used to cure many species of flu (Maugh, T., 1979)¹² and treat Parkinson's disease (Sonnberg, L., 2003)¹³, and polymers of adamantane have been approved as antiviral agents against HIV (Boukrinskaia, A. G., et al., 2009)¹⁴.

For the extraordinary properties of diamondoid molecules, the first attempt to artificially synthesized adamantane was in 1941 by Prelog and Seiwert¹⁵ but the result was not going as expected until there were several approaches promoted in the 1950s and 1960s. One of the most typical methods to construct lower diamondoids was the process of carbocation rearrangement (organic synthesis method). For the case of adamantane, the process initially hydrogenates cyclopentadiene to tetrahydrodicyclopentadiene with the catalysts of platinum dioxide (PtO₂) and diethyl ether (Et₂O), followed by the formation of adamantane after rearranging tetrahydrodicyclopentadiene with a strong Lewis acid (AlCl₃) as shown in Figure 1.3.



Figure 1.3: Schematic of adamantane synthesis

Until the early 1980s, higher diamondoids were successfully synthesized after numerous efforts to overcome the scarcity of adequate forerunners and catalysts including the constantly expanding number of potential isomers, the trapping of intermediates in minimal local energy, and the creation of undesired side products. Nevertheless, the progress was still very complicated and inefficient.

Micro-plasmas, which apply electric spark and pulsed laser plasmas (PLP) generated in supercritical fluids (SCFs) at high pressure, were alternative methods to build up diamondoids. In the former method, the reactor was made up of merged silica tubes whose inner and outer nominal diameters (ND) of 700 and 850 μm , respectively, which acted as fluidic routes and dielectric boundaries. Two electrodes are separated by a dielectric barrier in the electrode geometry. The outer, ground electrode in this example was made of an indium tin oxide (ITO) fine sheet. The high-voltage electrode was a tungsten film (with ND of 500 μm) placed into the capillary. The fluid temperature in the micro-capillary reactors was modified by subjoining the capillary and altering the temperature of the shield ranging from 279.2 - 284.8 K, which corresponds to the interval of the reduced temperature $T/T_{\text{crit}} = 0.964 - 0.983$ for xenon ($T_{\text{crit}} = 289.75 \text{ K}$, $p_{\text{crit}} = 5.84 \text{ MPa}$). A minor product of adamantane ($24.8 \pm 0.4 \text{ mg}$) was added to the fluid as a catalyst before injecting high-pressure xenon (5.83 - 5.99 MPa; $p/p_{\text{crit}} = 0.998 - 1.026$) through the cell. Syringe pumps are frequently used to modify pressure values because they allow for pressure control while also obtaining suitable flow rates for micro-reactor systems. In particular, the use of a syringe pump in a continuous-flow process achieves 0.05, 0.1, and 0.5 ml/min flow rates that result in reaction periods of 100, 50, and 10

min, respectively. The discharges were caused by a sine HV signal. A 10 kHz and 3.95–6.02 kVp-p (peak-to-peak) sine signal flux were employed to achieve the plasma.

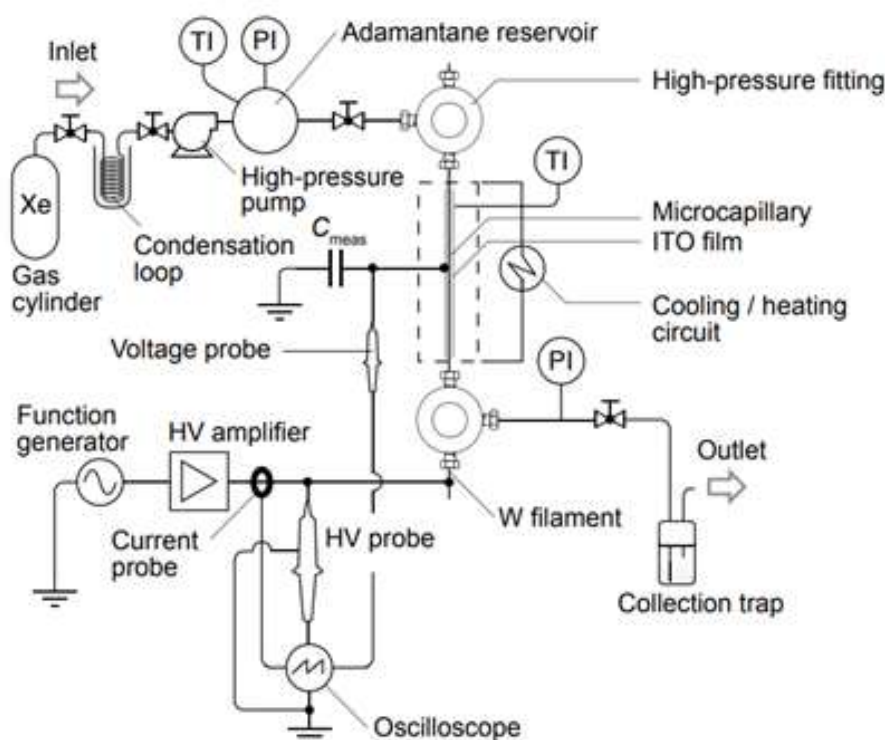


Figure 1.4: Process flow diagram of electric discharge in SCFs to synthesize diamondoids

Vietnamese-German University

However, the aforementioned methods do not consistently generate the products between higher or lower diamondoids. This is due to the fact that only diamondoids having stable energy can get through the reaction. For instance, most tetramantanes failed to develop into pentamantanes, whereas pentamantanes were not likely to generate tetramantanes.

Since the 1960s, with the introduction of Ruby lasers, the latter method using plasma that is induced by irradiation mechanism has been applied. In the 2010 - 2011 period, Nakahara et al.,^{16,17} employed pulsed laser ablation (PLA) in supercritical CO₂ (scCO₂) for the synthesis of diamondoids. Particularly, a 3 mL high-pressure cell (Figure 1.5) and a highly oriented pyrolytic graphite (HOPG) target were put in a high-pressure cell of the batch model (with 3 cm³ of inner volume). Over 99% purified adamantane was decomposed in scCO₂ with and without cyclohexane used as a solvent. The concentrated CO₂ was created by condensing the CO₂ gas with a purity larger than 99.995% in a distillation loop and subsequently placed it into the inner cell after chilled by liquid nitrogen. The HOPG targets in both scXe and scCO₂ were ablated with a second-harmonic neodymium-doped yttrium aluminum garnet (Nd:YAG) laser (with $\lambda = 532$ nm). Maximum fluence about 18 J.cm⁻² was generated on the exterior of the HOPG target by 7 mJ maximum energy for each pulse and its bandwidth and repeat rate were 7 ns and 10 Hz, respectively. The ablation experiments lasted for 60 minutes. The gas effluent from the cell after the reaction is guided through a trap containing 10 mL of cyclohexane from which the diamondoid products were collected.

The major drawback of the above plasmas approach is the requirement of specific high-pressure equipment. Therefore, an alternative method using atmospheric pressure micro-plasma reactors was developed.

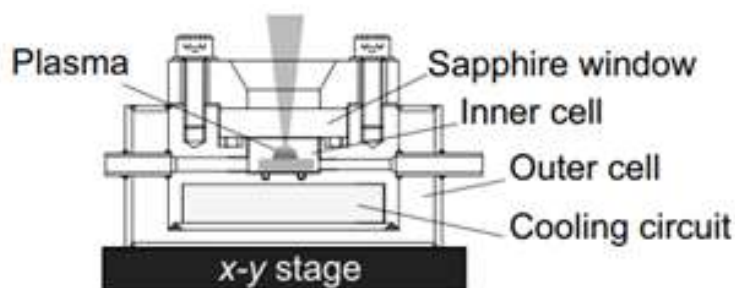


Figure 1.5: Side view of the high-pressure cell

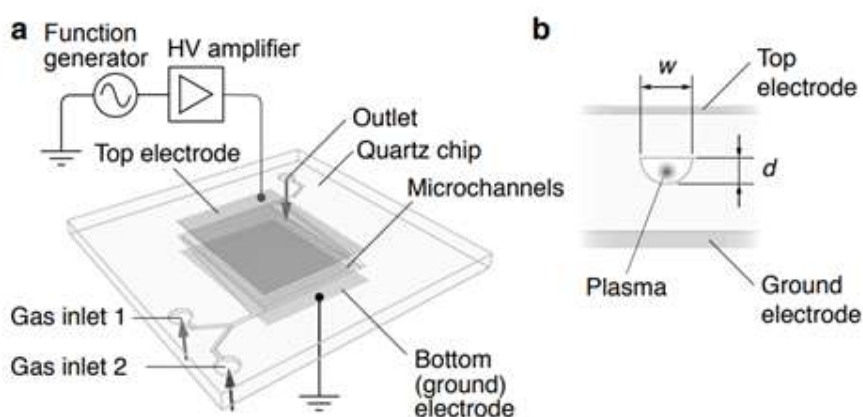


Figure 1.6: (a) Three-dimension of a micro-reactors. (b) Cross area of a single micro-reactor channel.



Vietnamese-German University

The main improvement was dielectric barrier discharge (DBD) plasma micro-reactors with a steady flow at atmospheric pressure that involves the utilization of methane (CH_4) and hydrogen (H_2) to ordinary chemical vapor deposition (CVD) (Bachmann et al., 1991)¹⁸ together with adamantane as a seed and catalyst. A 10 kHz frequency and peak-to-peak voltages among 3.2 - 4.3 kVp-p were applied during the experiments for 120 - 240 minutes. A trap stored with cyclohexane was first used to collect the gas and the synthesized diamondoids, then products were gathered by a solid phase removal filter. The cyclohexane was pumped through the entire system to flush the tubes and the micro-reactor after the experiment. It was the same with the solid-phase extraction filter but in a separate process and the solutions were then collected. To enhance the density of the outputs, the cyclohexane was vaporized on an 85°C plate before resolving the products with 1 mL of cyclohexane. Gas chromatography-mass spectrometry (GC-MS) was used to characterize the gathered materials. In conjunction with total ion chromatograms (TICs), selected ion monitoring (SIM) chromatograms relating to diamondoids' molecular masses in the mass-to-charge (m/z) range of 136 - 600, as well as those of potential chemical intermediates up to m/z 300, were obtained. The retention periods of peaks in the TIC and SIM figures were examined in comparison with those of diamondoids and derivatives separated from crude oil together with comparing the new mass spectra data to the reference one (NIST/EPA/NIH Mass Spectral Library (EI), 2012) to identify the possibility of chemical intermediates (Liang et al., 2012)¹⁹. The outcomes demonstrated that there was an ability to synthesize diamondoids at atmosphere pressure but with lower efficiency than earlier approaches conducted with high-pressure conditions and SCFs.

To increase the productivity of getting diamondoids and derivatives, it is critical to

developing methods for isolating and separating diamondoids found in petroleum and extractable organic matter (EOM). Dahl et al.²⁰ presented an approach to decompose non-diamondoids at high temperatures from condensates containing higher diamondoid distillate fractions, followed by reverse-phase liquid chromatography and then separated the higher diamondoids using distillation with acetone. Although this method allows for the pyrolysis of non-diamondoids, it does not guarantee that the high-order diamondoids are not destroyed throughout the process (Nguyen and Philp, 2016)²¹. He et al.²² proposed a new approach for CSIA analysis using a modified molecular sieve to get lower diamondoids from crude oils and rock extractable organic matter (EOM) (2012). Nevertheless, the isolation mechanism has not been well understood (Nguyen and Philp, 2016)²¹. In 2011, Huang et al.²³ described a saturated fractions chromatography process that relies on the adsorption-desorption separation by molecular distinguishing with β -cyclodextrin. The method was demonstrated to be efficient providing the oils had a sufficient high quantity of diamondoids relative to non-diamondoids, such as cycloalkanes. Nevertheless, it was not assured that the approach would operate equally well with oils that commonly contain a low concentration of diamondoids in coexistence with the dominating non-diamondoids. More recently, the lower diamondoids were successfully separated from oils using the commercial β -zeolite with the appropriate heat treatment condition (Nguyen and Philp, 2016)²¹.

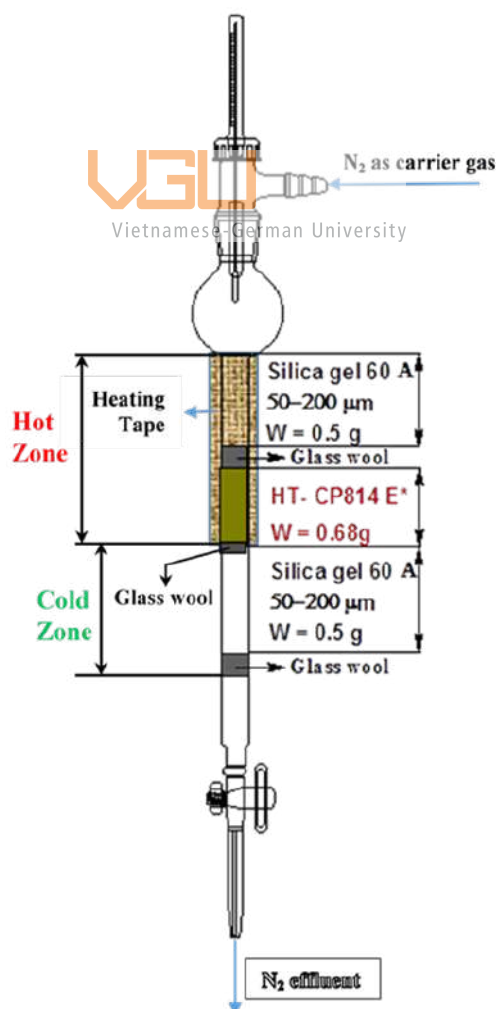


Figure 1.7: Schematic two-segment column for diamondoid separation

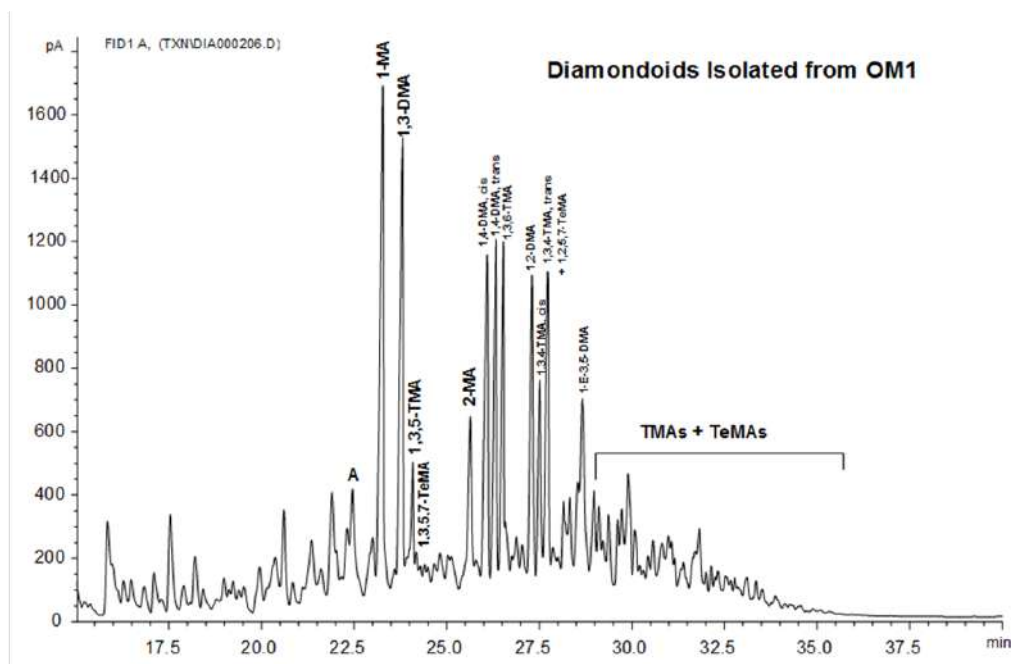


Figure 1.8: GC trace of adamantane and methylated derivatives separated from sample OM1 using two-segment column (HT-CP814 E°)

Hence, a good understanding of the molecular sieving effect is essentially crucial to achieving the rational design of molecular sieving membranes for diamondoid separation. In this regard, (Jiménez-Cruz and García-Gutiérrez, 2020)²⁴ determined critical molecular dimensions of the adamantane, diamantane, and their methyl derivatives in the two-dimensional pore models using the quantum mechanical modeling. Despite the importance of the critical molecular dimensions and shape, they will not enable to capture faithfully the dynamics of the molecular sieving effect due to less well-defined molecular geometry at the nanoscale as well as the importance of molecular alignment at pore entry and inside pore body. Hence, the molecular dynamics (MD) simulation method is well-suited to elucidate the underlying mechanism of the mixture adsorption separation including the molecular sieving effect.

In this thesis, the Large-scale Atomic/Molecular Massively Parallel Simulator (LAMMPS)²⁵ was used to simulate the adsorption dynamics of the lower-diamondoids in the mixture of benzene and 2,2-dimethyl hexane (22DMC6) in the adsorbent models (activated carbons and β -zeolite). To capture the molecular sieving effect, benzene and 22DMC6 were selected to represent typical aromatic compounds and iso-alkane in the light hydrocarbon fraction (C4-C7) of oils that contain mainly the lower diamondoids. The exclusion of the diamondoids by the β -zeolite is indicative of preferential adsorption of the non-diamondoids (aromatics, cycloalkanes, and iso-alkanes) (Nguyen and Philp, 2016)²¹. Hence, the 22DMC4 (or 22DMC5, 22DMC6) with a quaternary carbon atom bonded to four other carbon atoms is expected to have the largest steric hindrance to pore entrance. Interpretation of the molecular sieving effect was conducted based on the MD simulated self-diffusion coefficients and the simulated snapshots obtained by the visual molecular dynamics (VMD) package²⁶.

Methodologies and materials

2.1 Molecular dynamics simulation principle

Molecular Dynamics (MD) simulation is an approach for predicting the phase equilibria, transport phenomena, and coexistence properties of an N-particle system by numerically generating Newtonian motion equation²⁷. In particular, all particles in the system have their initial locations and velocities assigned at the start of the simulation. The Maxwell-Boltzmann distribution²⁷ is employed to specify the initial particle velocities. The forces, coordinates, and velocities of atoms are determined at each time step, under a specific interatomic potential model, with the applied periodic boundary condition (PBC).

The force \vec{F}_i acting on each atom based on the Newtonian second law is calculated as follows:

$$\vec{F}_i = -m_i \vec{a}_i = -m_i \frac{d^2 \vec{r}_i}{dt^2} = -\nabla_i U(\vec{r}_1, \vec{r}_2, \dots, \vec{r}_N)$$

where m_i , \vec{a}_i , and $U(r)$ are the mass, acceleration, and potential energy of the i th particle, with $i=1, \dots, N$.

For pairwise additivity of the potential assumed, the interatomic potential $U(r)$ is given as:

$$U(r) = \frac{1}{2} \sum_{j \neq i}^N u(r_{ij}) \quad (2.1)$$

where $u(r)$ is the pair interaction potential.

After obtaining the atomic forces \vec{F}_i at the current time step, new coordinates and velocities at the next time step are predicted using Velocity-Verlet (VV) integrator. The VV algorithm can be summarized with the following steps

Step 1: Predict the new atomic positions $\vec{r}_i(t + \Delta t)$ at the time $t + \Delta t$ from the current atomic velocities $\vec{v}_i(t)$, positions $\vec{r}_i(t)$, and forces $\vec{F}_i(t)$

$$\vec{r}_i(t + \Delta t) = \vec{r}_i(t) + \vec{v}_i(t)\Delta t + \frac{1}{2} \frac{\vec{F}_i(t)}{m_i} \Delta t^2 \quad (2.2)$$

Step2: Update the current atomic velocities at an intermediate time step $(t + \Delta t/2)$

$$\vec{v}_i(t + \frac{\Delta t}{2}) = \vec{v}_i(t) + \frac{1}{2} \frac{\vec{F}_i(t)}{m_i} \Delta t \quad (2.3)$$

Step3: Compute the new atomic forces $\vec{F}_i(t + \Delta t)$ at the time $(t + \Delta t)$ from new atomic coordinates $\vec{r}_i(t + \Delta t)$ obtained at the step 1:

$$\vec{F}_i(t + \Delta t) = -\vec{\nabla}_i U(\vec{r}_i(t + \Delta t)) \quad (2.4)$$

Step4: Update the new atomic velocities at the time $(t + \Delta t)$:

$$\mathbf{v}_i(t + \Delta t) = \mathbf{v}_i \left(t + \frac{\Delta t}{2} \right) + \frac{1}{2} \frac{\mathbf{F}_i(t + \Delta t)}{m_i} \Delta t \quad (2.5)$$

2.2 Force field

There are two main ways to calculate energy: quantum-mechanics (QM) based methods to calculate the electronic structure of a molecule using molecular orbital (MO) theory, and molecular mechanics (MM) based methods or force field methods based on empirical potential energy functions²⁷. Despite the high predictive accuracy of the QM approach, which normally requires extensive computation demand, the empirical force field method is more commonly used, especially the complex models that are impractical to be analyzed by the QM approach. In the force field approach, the potential energy is determined from different elements of the bonded and non-bonded forces in the structure.

The simplest form of potential to represent intermolecular interaction within the molecules is called atom-atom potential, and is written as

$$U(r) = \sum_{i=1}^{N_a} \sum_{j=1}^{N_b} \phi_{ij}(r_{bj} - r_{ai}) + V_{elect} \quad (2.6)$$

where ϕ_{ij} is a potential function appropriate for the types of atoms i and j , r_{ai} is the position of the i th atom on molecule a , r_{bj} is the position of the j th atom on molecule b , and V_{elect} is the electrostatic energy between the molecules. A simple form for ϕ_{ij} is given by Lennard Jones (LJ) potential:

$$\phi_{ij}(r) = 4\epsilon_{ij} \left[\left(\frac{\sigma_{ij}}{r_{ij}} \right)^{12} - \left(\frac{\sigma_{ij}}{r_{ij}} \right)^6 \right] \quad (2.7)$$

where σ_{ij} , ϵ_{ij} , and r_{ij} are Lennard-Jones cross-collision diameter, cross-well depth, and distance between the interacting sites, respectively, for the pair atoms i and j .

Lorentz-Berthelot combining rules are used for the interaction parameter between unlike pairs:

$$\sigma_{ij} = \frac{1}{2}(\sigma_{ii} + \sigma_{jj}) \quad (2.8)$$

$$\epsilon_{ij} = (\epsilon_{ii}\epsilon_{jj})^{\frac{1}{2}} \quad (2.9)$$

Coulomb's law between any two charges q_i and q_j is used to demonstrate the electrostatic interaction energy between the non-bonded atoms in the system as follows:

$$V_{elect} = \sum_{i=1}^{N_a} \sum_{j=1}^{N_b} \frac{q_i q_j}{4\pi\epsilon_0 r_{ij}} \quad (2.10)$$

where there are $N_a(N_b)$ charges on molecule $a(b)$, q_i is the charge on the i th charge on molecule a , and q_j is the charge of the j th atom on molecule b .

Bond stretching, valence angle bending, dihedral angle bending, and improper angle bending are the four primary types of intramolecular energy expressions that illustrate the interaction between pairs of bonded atoms.

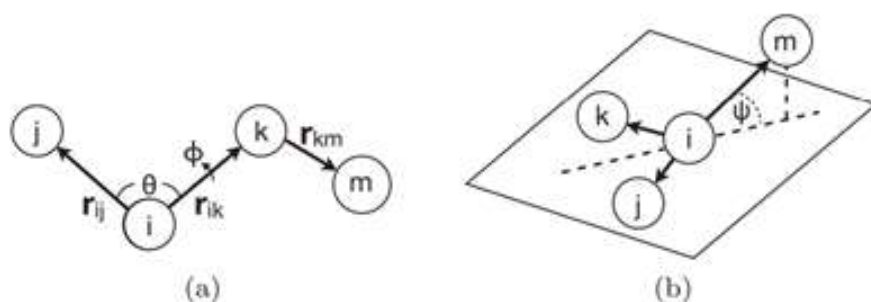


Figure 2.1: Bond distances and angles in intramolecular potentials

Consider the bond between atoms i and j in the Figure 2.1. The instantaneous length of that bond is $r_{ij} = |r_{ij}|$, while its equilibrium length is denoted as $r_{ij,0}$. The energy of a bond can be written as

$$U(r_{ij}) = \frac{k_{ij}}{2}(r_{ij} - r_{ij,0})^2 + \frac{g_{ij}}{2}(r_{ij} - r_{ij,0})^3 + \frac{h_{ij}}{2}(r_{ij} - r_{ij,0})^4 + \dots \quad (2.11)$$

where k_{ij} , g_{ij} , and h_{ij} are the force constants of the bond. In the harmonic approximation, the energy of a bond is simplified to the first term in the equation above with the $r_{ij,0}$ denote the equilibrium bond length.

Hooke's law (also known as harmonic potential) is frequently used to describe angle variations from their equilibrium values

$$U(\theta) = \frac{k_{ijk}}{2}(\theta_{ijk} - \theta_{ijk,0})^2 \quad (2.12)$$

Where $\theta_{ijk,0}$ is the equilibrium angle and k_{ijk} is the force constant.

The dihedral angle ϕ , also called torsional angle, is defined as the angle between the normal to the planes containing atoms j_{ik} and i_{km} in Figure 2.1. The torsional energy associated with non-bonded interactions between atoms separated by three bonds (1,4 interactions) can be written as a Fourier series for each dihedral angle:

$$V(\phi) = \frac{V_1}{2} [1 + \cos(\phi + f_1)] + \frac{V_2}{2} [1 - \cos(2\phi + f_2)] + \frac{V_3}{2} [1 + \cos(3\phi + f_3)] \quad (2.13)$$

where the parameter $V_{1(2,3)}$ is called barrier height, $f_{1(2,3)}$ are the phase factors that determine the location where the torsional angle value reaches the minimum.

The inversion angle ψ is a so-called improper torsion angle that describes the energy associated with the arrangement of three atoms around a central one. ψ is the angle between the bond vector r_{im} and the plane containing the other three atoms (or out-of-plane angle bending). Harmonic potential as well as planar potentials are typically used to represent the energy of this motion:

$$U(\Psi_{ijkm}) = A \cos(\Psi_{ijkm} + \delta) \quad (2.14)$$

However, in this study, this type of energy is not taken into account to make the simulation simpler.

There is a more applicable method that can describe the phase behavior of hydrocarbons and related compounds especially branched alkanes called the united-atom or coarse-grained model. In this model, for example, the hydrogens on a methyl group are combined with the carbon atom and the $-\text{CH}_3$ unit is represented by a single center of force as in the figure below. This model will reduce the number of interacting particles in the methyl group from 4 to 1, with a proportional decrease in the computational burden. This approximation introduces additional inaccuracy, but the gain in speed due to the fewer interactions allows for the study of such complex systems.

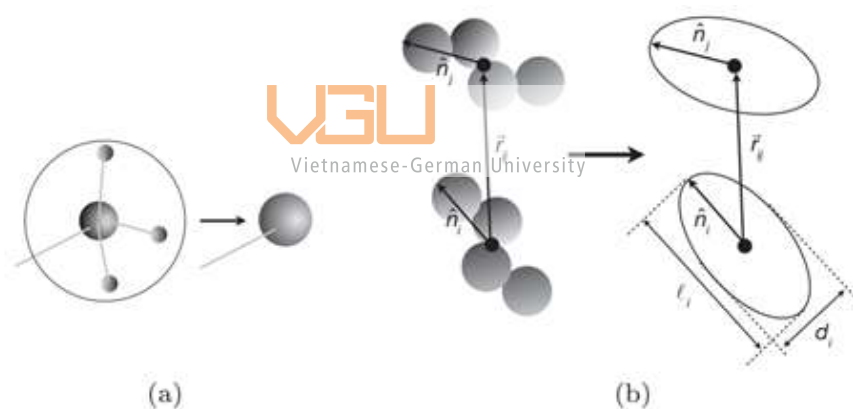


Figure 2.2: Coarse-grained potential illustration. (a) A methyl group ($-\text{CH}_3$) is simplified as a single point of interaction. (b) A united-atom potential of the atoms in a small chain.

2.3 Molecular dynamics analysis

2.3.1 Means square displacement (MSD)

The tendency of approaching the equilibrium state of matter by moving to eliminate spatial diversity in the composition is called diffusion²⁸. Brownian molecular motion (self-diffusion or random walk) is a rapid and random movement. It is described by the time dependence of concentration distribution or the MSD of diffusants. As the result of statistical physics, Einstein's relation shows that MSD is related to the diffusion coefficient:

$$\langle r^2(t) \rangle = 6Dt \quad (2.15)$$

And the macroscopic law that describes diffusion is known as Fick's first law:

$$J = -D \frac{\partial c}{\partial z} \quad (2.16)$$

where J is the diffusive flux, D is the self-diffusivity (or diffusion coefficient), and c is the concentration. A detailed interpretation of the formulas is shown in Appendix A. The self-diffusion coefficient D_s indicates atomic flexibility. The higher the value of D_s , the faster substances bypass adsorbents. In other words, the ratio between self-diffusion coefficients reveals the selectivity of adsorbates by the adsorbent. After collecting the MD trajectories including positions ($\mathbf{r}_i(t)$) and velocities ($\mathbf{v}_i(t)$) of all particles in the system at different times, for each particle in the timeline, the MSD data is then measured using the first MD trajectory as follows:

$$\langle r_1^2(\Delta t) \rangle = \frac{1}{N_{time}} \sum_{i=1}^{N_{time}} (r_1(t_0 + i\Delta t) - r_1(t_0))^2 \quad (2.17)$$

Then the average distance of an N-particle system is calculated as:

$$\langle r^2(\tau) \rangle = \frac{1}{N_{particle}} \frac{1}{N_{time}} \sum_{i=1}^{N_{particle}} \sum_{j=1}^{N_{time}} (r_i(t_0 + \tau) - r_i(t_0))^2 \quad (2.18)$$

With $\tau = i\Delta t$

Finally, D_s is measured by fitting the linear curve of MSD vs time with Einstein's relation.

2.3.2 Velocity autocorrelation function

In the second approach, the diffusion coefficient D_s is measured through velocity autocorrelation function (VACF), which is directly calculated from MD time-dependent velocity as follows²⁸:

$$\Delta r(t) = \int_0^t v(t') dt' \quad (2.19)$$

After detailed integration and combination in Appendix B, we get

$$D = \int_0^\infty d\tau \langle v_x(\tau) v_x(0) \rangle \quad (2.20)$$

With the same format to calculate D as MSD but using the second MD trajectory – velocity $v_i(t)$ yields:

$$D = \frac{1}{N_{particle}} \frac{1}{N_{time}} \sum_{i=1}^{N_{particle}} \sum_{i=1}^{N_{time}} (v_i(t_0 + \tau) \cdot v_i(t_0)) \quad (2.21)$$

2.3.3 Radial distribution function

The radial distribution function (RDF) evaluates the probability of locating a molecule at a distance r from a centered molecule, therefore, it is very helpful to determine the structure of materials. As a consequence, RDF is simply the ratio of local density to bulk density of material²⁹. Accordingly, simulated RDF is determined from a set of equilibrium microscopic configurations

$$g(r) = \frac{\sum_{k=1}^M N_k(r, \Delta r)}{M \left(\frac{1}{2}N\right) \rho V(r, \Delta r)} \quad (2.22)$$

where the outcome of the counting operation (C.9) at time t_k in the run is denoted by N_k (also determined as the number of particles within the spherical shell, M is the number of cells, Δr is the shell thickness. ρ is the bulk density of the substance. $V(r, \Delta r)$ is the spherical volume. $g(r) = 0$ when the separation is less than about one diameter value of an atom and $g(r) = 1$ if the separation in the fluid is too large to have the changing in the position of two atoms.

$g(r)$ is a sequence of δ -symbols for atoms fixed onto the sites of typical crystalline patterns such as face-centered cubic (fcc), body-centered cubic (bcc), and hexagonal closest packed (hcp). The $g(r)$ plot differences allow us to discriminate between these two structures; for instance, the fcc lattice has fewer atomic clusters separated by $\sqrt{2}$ but more pairs separated by $\sqrt{3}$ than the simple cubic lattice. Because typical crystalline solids have a structure that repeats itself on a regular basis, the one-dimension quantity $g(r)$ is adequate for distinguishing between distinct three-dimension architectures.

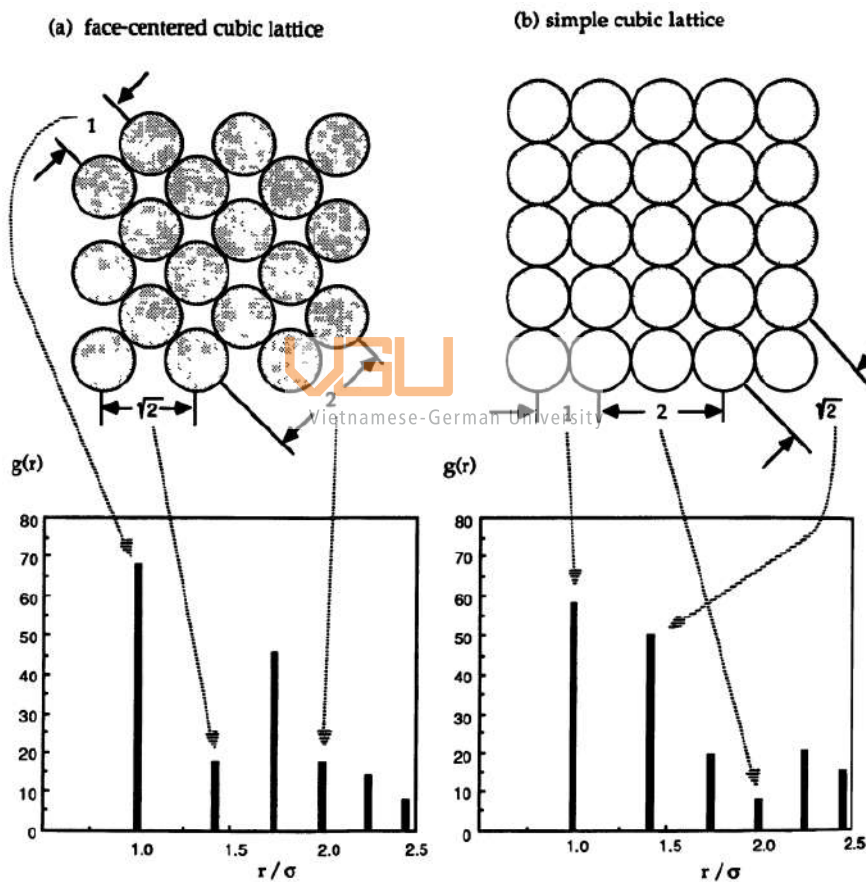


Figure 2.3: (a) Structure of a close-packed fcc lattice computed for 108 atoms and periodic boundary conditions. (b) Structure of a close-packed simple cubic lattice computed for 125 atoms and periodic boundary conditions.

$g(r)$ behaves substantially differently in crystalline solids than it does in low-density gases. Atoms interact with one another in a gas mostly by binary collisions, and no more than weak local structures develop around any given atom. The low-density limit of $g(r)$ is provided by

$$\lim_{\rho \rightarrow 0} g(r) = \exp \left[-\frac{u(r)}{kT} \right] \quad (2.23)$$

where $u(r)$ is the bonded interaction energy function. The plot of this low-density limit is shown below

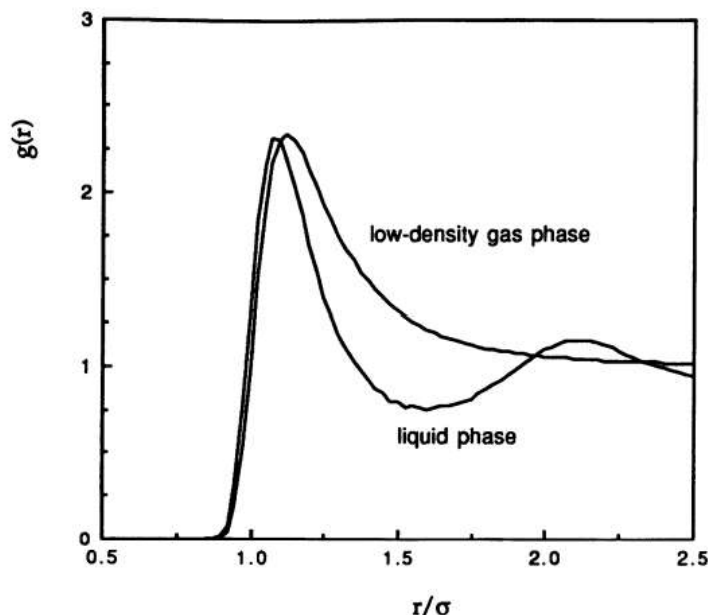


Figure 2.4: Radial distribution function for gas and liquid phases of the Lennard-Jones fluid

The plot of $g(r)$ in liquids and amorphous solids is midway between that of a crystalline solid and a gas; liquids display short-range arrangement comparable to that of a crystal but long-range disarrangement similar to that of gases. Due to the different performances of $g(r)$ based on the state of each material, it can be another indicator to evaluate the selectivity of adsorbents. The data relating to each adsorbate, which is close to the gas phase, show less time it travels in the adsorbent. This suggests a strategy to capture the substance based on its time travel.

2.4 Materials

2.4.1 Adsorbents

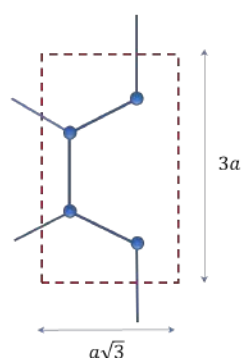
a. Graphitic Slit-like Pore Configuration

The configuration of graphene is created from its unit cell, as shown in Figure 2.5. Then it is used for building up a graphitic slit-pore model, as depicted in Figure 2.6. In this study, the graphitic pore walls comprise four graphene layers with an interlayer spacing distance of 0.335 nm as the periodic boundary condition is applied. The unit cell of the graphitic pore walls contains 1344 atoms with dimensions of 2.93 nm \times 2.96 nm \times H_{in} . H_{in} is the internal pore width and is defined as

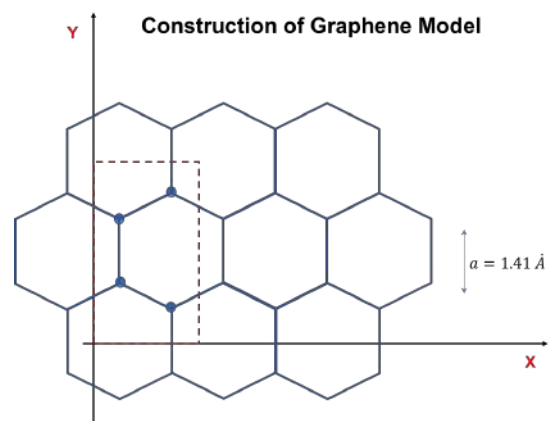
$$H_{in} = H_{cc} - \sigma_c \quad (2.24)$$

where $\sigma_c = 3.4 \text{ \AA}$, $\epsilon_c = 28 \text{ K}$, $q_c = 0$ and H_{cc} is physical pore width measured from carbon center to carbon center.

Unit Cell of Graphene

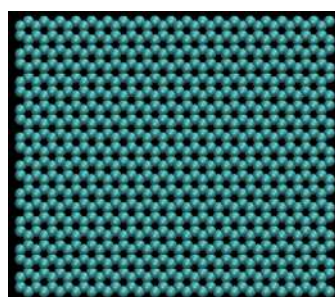


(a)



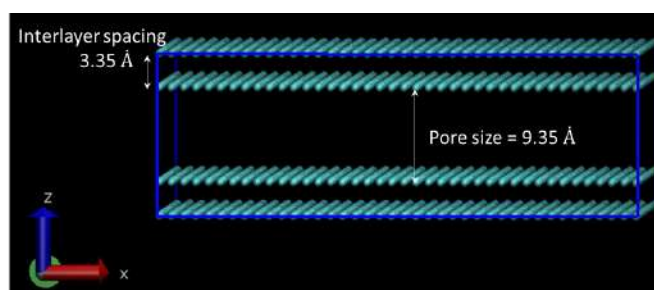
(b)

Figure 2.5: Unit cell and construction of graphene model



Top View

(a)



Front View

(b)

Figure 2.6: Configuration of graphitic slit-pore model

b. Realistic Porous Carbon Structure (the activated carbon fiber ACF-15)

Despite the ideal slit-pore structure is widely accepted to represent the micro-model of porous carbons, it does not truly capture the real adsorption behavior in equilibrium and dynamics state in nano-porous carbons due to its lack of the curvature of defective carbon surfaces as well as disregard of the pore network accessibility which involves in the retardation or hindrance of adsorbate molecules to enter molecularly restricted pore entrances formed from the curved carbon surfaces. Furthermore, the irregular shape of pore bodies with the complex potential landscape induces very different adsorption behaviors from those in the graphitic pores. In our previous works (Nguyen et al., 2008)³⁰, the distinct adsorption behaviors were shown for common gases (Ar, N₂, CH₄, CO₂), and water using the realistic carbon design of activated carbon fiber ACF-15. The ACF-15 model was previously built using Hybrid Reverse Monte Carlo (HRMC) approach (Nguyen and Bhatia, 2011)³¹. In this study, the realistic carbon structure of ACF-15 is used to examine the adsorption equilibrium and dynamics of lower diamondoids and other hydrocarbons (isoalkanes and benzene) in comparison with those in the graphitic slit-pore structure. The study aims to assist in seeking the rational microstructure of nanoporous materials for the separation task of diamondoids from oils. In general, the HRMC model of ACF-15 contains a periodic unit cell of 1166 carbon atoms together with four zones (1, 2, 3, and 4) corresponding to four pore size ranges (6.8-8 Å, 8.9-10.4 Å, 11.4-12.4 Å, and 12.9-13.9 Å, respectively)³¹, and its unit cell measurements are 2.95 nm x 2.98 nm x 3.02 nm³⁰. The unit cell of the HRMC model of ACF-15 and its pore

size distributions are reproduced in Figure 2.7.

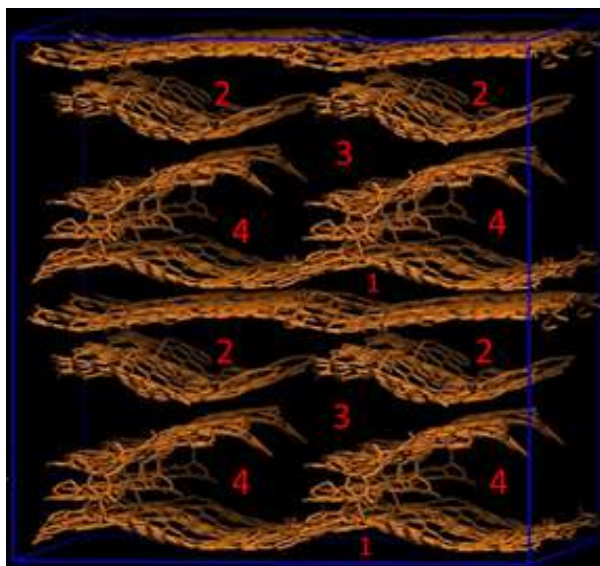
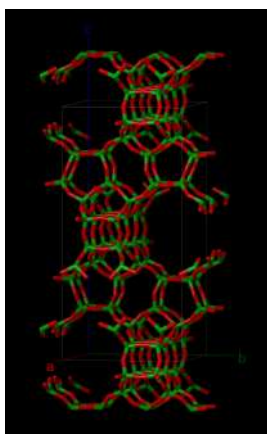


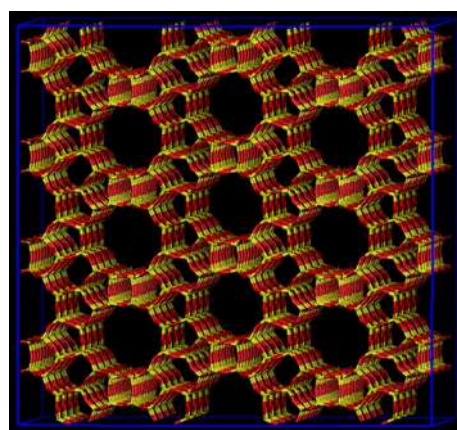
Figure 2.7: Snapshot of ACF-15

Subsequently, the HRMC model is placed in a larger cubic box to form a new unit cell that can accommodate fluids outside the solid carbon structure. The newly constructed unit cell enables to investigate the pore accessibility of fluid atoms to the solid carbon structure during MD simulations. The ACF-15 configuration is considered to be rigid. The Lennard Jones (LJ) potential was used to represent the carbon atoms with fluid atoms. LJ parameters for the carbon-carbon interactions are taken from Nguyen et al.³⁰ with $\sigma_C = 3.4 \text{ \AA}$, $\epsilon_C = 36 \text{ K}$, $q_C = 0$.

c. β -zeolite



(a)



(b)

Figure 2.8: Structure of β -zeolite. (a) The unit cell of beta polymorph A. (b) Supercell of β -zeolite.

In this thesis, polymorph A, whose unit cell is tetragonal with lattice constants of $12.66 \text{ \AA} \times 12.66 \text{ \AA} \times 26.41 \text{ \AA}$, was selected to obtain the β -zeolite structural model. Particularly, the CIF

file of the polymorph A was taken from the Database of Zeolite Structure website³² as shown in Figure 2.8a. Subsequently, we modified the CIF file using the VESTA software³³ to generate the PDB file of the unit cell. Then this PDB file was used to create the corresponding PSF file by Visual Molecular Dynamics (VMD) software package. The PSF file is the protein structure file that contains the atomic connectivity information (e.g. bond lengths and bond angles) and atomic charges while the PDB file is the protein data bank file that contains atomic coordinates. Eventually, the unit cell was further replicated to construct the supercell with dimensions of 50.664 Å x 50.664 Å x 52.812 Å, as depicted in Figure 2.8b. The final atomic configuration of zeolite beta contains 4096 Si atoms and 7264 O atoms. The zeolite model is assumed to be rigid. Charges of Si and O atoms are taken from Coulombic point-charge interaction between partially charged atoms on the zeolite and partially charged of guest molecules (V.T. Nguyen et al., 2014)³⁴. LJ potential is utilized to represent the interatomic interaction strength among the O atoms and O atoms with fluid atoms. LJ parameters (well-depth ϵ and collision diameter σ) for the O-O interaction is taken from that of FAU zeolites ($\sigma_O = 3.0$ Å, $\epsilon_O = 93.53$ K, $\sigma_H = 0$ Å, $\epsilon_H = 0$ K, $q_{Si} = 1.6$, and $q_O = -0.8$) (Di Lella A. et al., 2006)³⁵.

2.4.2 Adsorbates

a. Diamondoids

Cartesian carbon coordinates of adamantane and diamantane are first generated in the xyz files using the unit cell of the diamond structure. Subsequently, hydrogen atoms are added to the carbon model of adamantane and diamantane to obtain their all-atom structure of adamantane containing both hydrogen and carbon atoms. This step was carried out using the Open Babel program³⁶ to generate the xyz coordinate files with the atomic connectivity information. The xyz files of adamantane and diamantane were processed using the VMD software to generate the pairs of PSF and PDB files of the diamondoid models. The partial charges on the carbon atoms are assigned to obtain neutral molecules, where the charge of the attached hydrogen atom is +0.1 (W. L. Jorgensen et al., 1996)³⁷. The unit cell of adamantane has 10 carbon atoms and 16 hydrogen atoms with the dimensions of 0.6967 nm x 0.6967 nm x 0.6967 nm. And the diamantine unit cell has 14 carbon atoms and 20 hydrogen atoms with the dimensions of 0.7858 nm x 0.7858 nm x 0.7858 nm. The unit cells are presented in the following figures

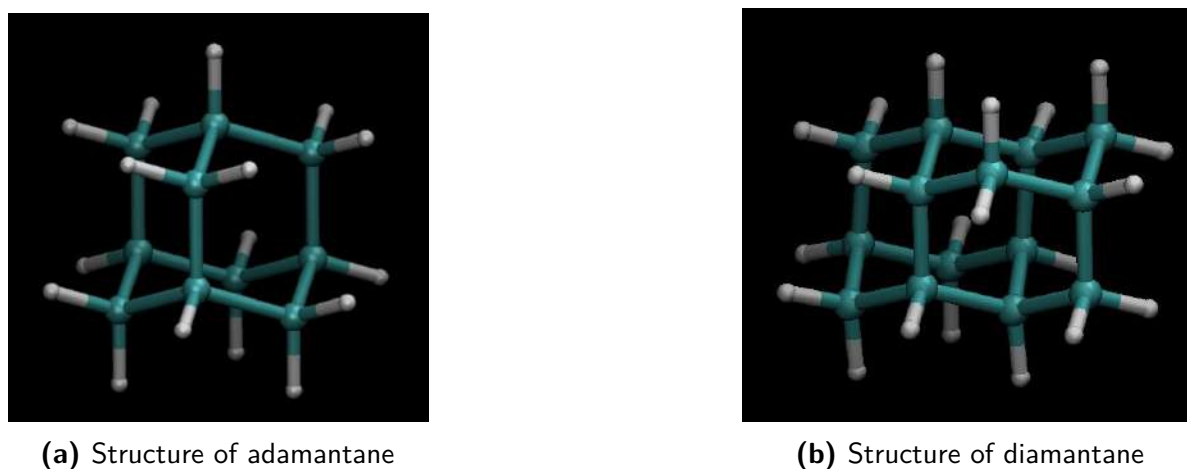


Figure 2.9: Structure of lower diamondoids

The tables below provide more information on the noncovalent potential energy parameters

and the LJ properties between sp^3 carbon and hydrogen atoms, which are extracted from the well-known OPLS force field (W. L. Jorgensen et al., 1996)³⁷. The equivalent values for C-H interactions are provided by Lorentz-Berthelot combination rules. And the partial charge was mentioned above.

Table 2.1: Non-bonded interaction energy parameters of diamondoids

General parameters	σ (Å)	ϵ (kcal/mol)
C, Adamantane ¹	3.5	0.066
C, Adamantane ²	3.4	0.1094
H, Adamantane ¹	2.5	0.033
H, Adamantane ²	2.649	0.0158

where 1 is for the first model of adamantane, methyl adamantane, and 1,3-dimethyl adamantane, and 2 is for the second model of adamantane

Table 2.2: Bonded interaction energy parameters of diamondoids

Bond	b_{eq} (Å)	k_b/k_B (K)		
C - C	1.529	268		
C - H	1.09	340		
Angle	θ_0 (°)	k_θ/k_B (K)		
C- C- C	112.7	58.35		
C- C- H	110.7	37.50		
H- C- H	107.8	33.00		
Dihedral	V_0/k_B (kcal/mol)	V_1/k_B (kcal/mol)	V_2/k_B (kcal/mol)	V_3/k_B (kcal/mol)
C- C- C- C ¹	0	0.870	0.0785	0.1395
C- C- C- H ¹	0	0	0	0.183
H- C- C- H ¹	0	0	0	0.159

1 is for methyl adamantane and 1,3-dimethyl adamantane

b. 2,2-dimethyl hexane (22DMC6)

The atomic model of the 22DMC6 alkane was constructed using Molecular Mechanical Force Field (MMFF) Toolkit website³⁸. In particular, MMFF Toolkit provides the tools to sketch the 2D-molecule structure of a molecule and generate the 3D-molecular structure in a mol2 file from its sketched 2D-atomic structure. Subsequently, the mol2 file is converted to the pair of PSF and PDB files of the alkane model using the VMD software.

The non-bonded energy between interaction sites, represented by a united-atom force field, is described by LJ parameters in linear alkanes NERD models (Nath et al., 1998³⁹; Nath and de Pablo, 2000⁴⁰). The LJ and intramolecular potential energy parameters for bare carbon atom is developed in branched alkanes NERD force field (S. K. Nath and R. Khare, 2001⁴¹) as tables below:

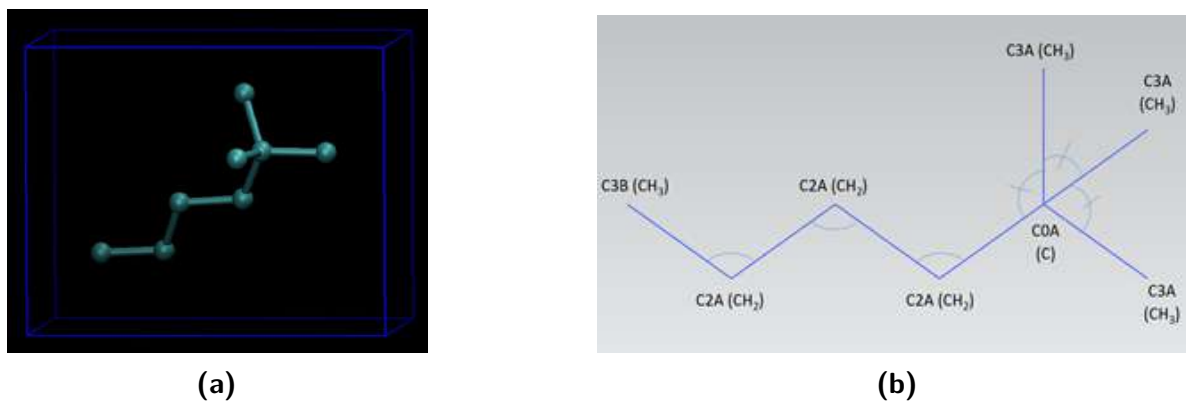


Figure 2.10: Structure of 22DMC6

Table 2.3: Non-bonded interaction energy parameters of alkanes

General parameters	σ (Å)	ϵ/k_B (K)
CH ₃ (C3B)	3.91	104
CH ₂ (C2A)	3.93	45.8
C (C0A)	3.91	17
CH ₃ (C3A)	3.87	74.5

Table 2.4: Bonded interaction energy parameters of alkanes

Bond stretching energy	b_{eq} (Å)	k_b/k_B (K)		
CH _x - CH _y	1.54	96500		
Angle bending energy	θ_0 (°)	k_θ/k_B (K)		
CH _x - (CH ₂) - CH _y	114	62500		
CH _x - (C) - CH _y	109.47	62500		
Dihedral bending energy	V_0/k_B (K)	V_1/k_B (K)	V_2/k_B (K)	V_3/k_B (K)
CH _x - (CH ₂) - (CH ₂) - CH _y ¹	0	355.4	-68.19	791.32
CH _x - (CH ₂) - (C) - CH _y ¹	0	0	0	1635.7

c. Benzene

The pair of PSF and PDB files of the benzene structure was generated with the same method used to obtain that of 22DMC6.

The Coulomb plus Lennard-Jones format is employed to describe the intermolecular interactions. LJ parameters and charge variables are collected as a result of Monte Carlo simulation for liquid benzene developed by American Petroleum Institute Research Project 44, 1953⁴². There are five parameters for benzene: ϵ and σ for carbon and hydrogen, and one charge variable since $q_C = -q_H = 0.115$. The resultant parameters are detailed in the tables below:

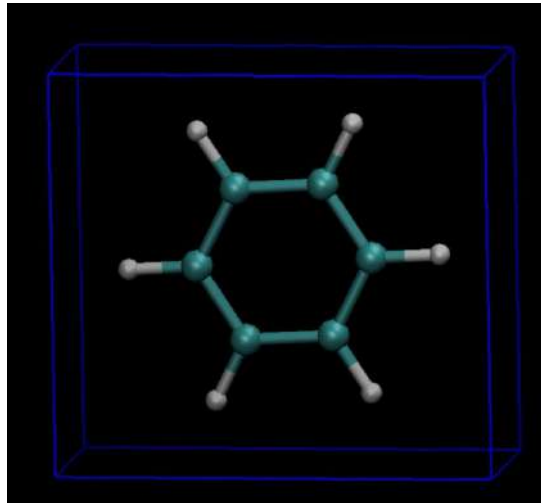


Figure 2.11: Structure of benzene

Table 2.5: Non-bonded interaction energy parameters of benzenes

General parameters	σ (Å)	ϵ (K)
C, Benzene	3.55	0.07
H, Benzene	2.42	0.03

Table 2.6: Bonded interaction energy parameters of benzenes

Bond type	b_{eq} (Å)	k_b/k_B (K)
C - C	1.40	600
C - H	1.09	400
Angle type	θ_0 (°)	k_θ/k_B (K)
C- C- C	120	35
C- C- H	120	35

Results and discussion

3.1 Adsorption dynamics in β -zeolite

Adsorption dynamics of pure hydrocarbons (adamantane (ADA), benzene (BZN), 2,2-dimethyl hexane (ALK)) and their mixture in β -zeolite (BEA) are analyzed using Large-scale Atomic/Molecular Massively Parallel Simulator (LAMMPS). For the study of separating lower diamondoids from oils, the hydrocarbon mixture simply represents the synthetic light oil fraction whose main compound groups are lower diamondoids, cyclic compounds, and isoalkanes presumably represented by adamantane, benzene, and 2,2-dimethyl hexane, respectively. ADA is a cage-like molecule with spatial molecular symmetry and the smallest member of the diamondoids family, BZN is a two-dimensional molecule with planar molecular symmetry while ALK is a non-symmetrical molecule whose head is the largest among alkanes. For molecular dynamics (MD) simulations, force fields of ADA, BZN, and ALK are presented in Tables 2.1 to 2.6.

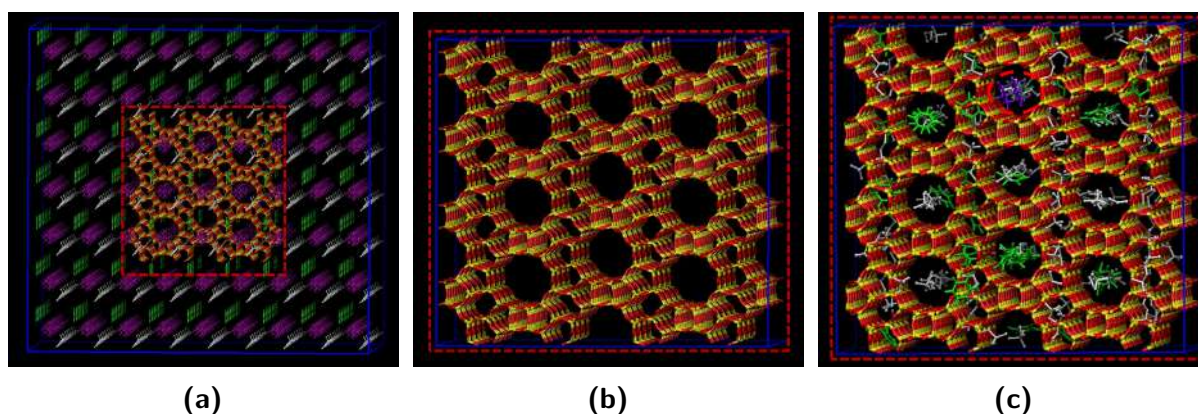


Figure 3.1: Investigation on adsorption accessibility of the synthetic oil to β -zeolite adsorbent. (a) MD initial configuration of the synthetic oil in β -zeolite. (b) MD initial configuration does not contain the synthetic oil in β -zeolite. (c) MD snapshot of the hydrocarbons inside β -zeolite after 3ns run.

For the MD simulation study of pore accessibility of the synthetic oil fraction to β -zeolite, we place 369 ADA molecules, 394 BZN molecules, and 393 ALK molecules on a lattice around the β -zeolite supercell to create the simulated MD unit cell as illustrated in Figure 3-1a.

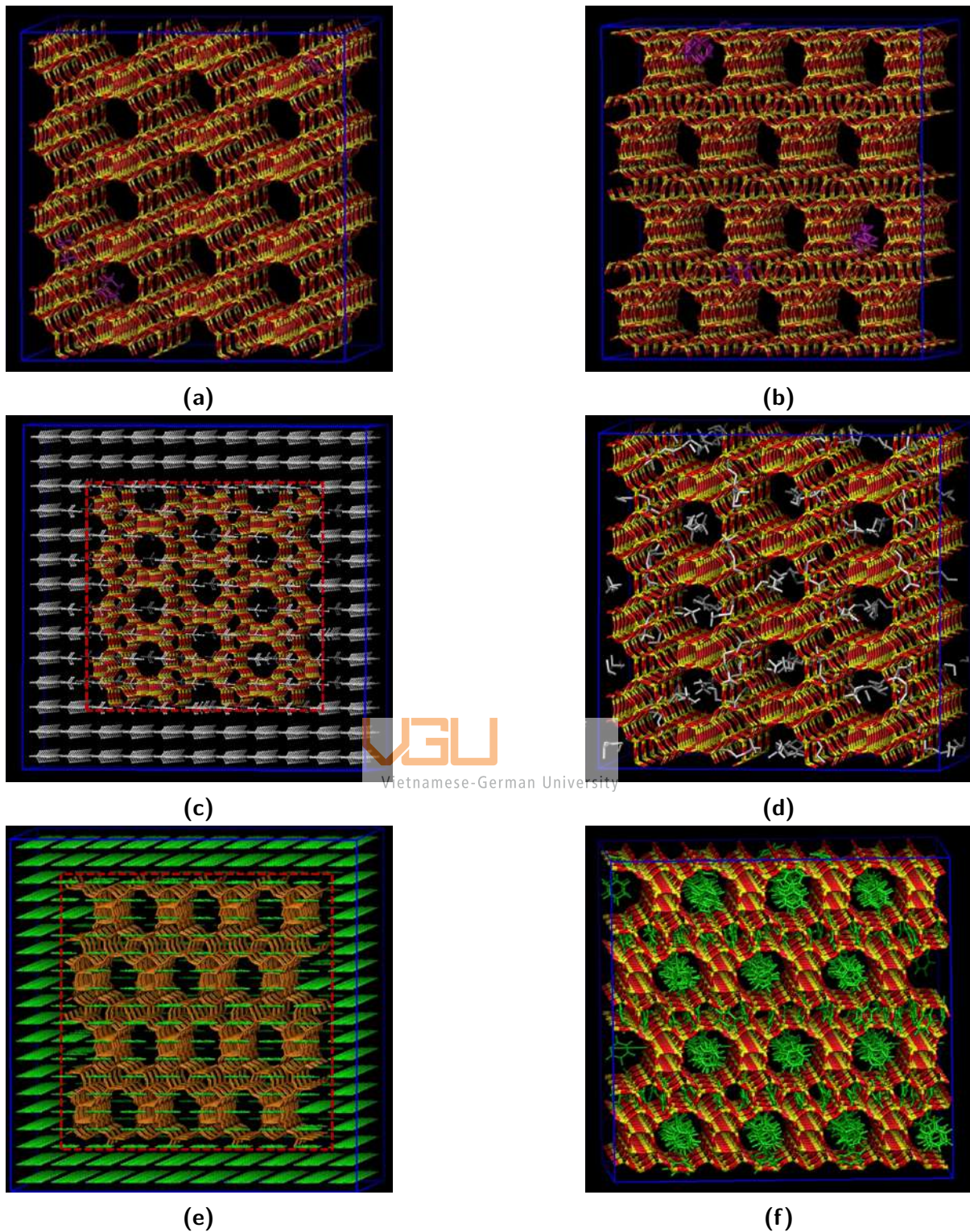


Figure 3.2: Investigation on adsorption accessibility of pure hydrocarbon to β -zeolite adsorbent. (c) MD Initial configuration of alkane in β -zeolite. (d) MD snapshot of alkane in β -zeolite. (e) MD Initial configuration of benzene in β -zeolite. (f) MD snapshot of benzene in β -zeolite.

Accordingly, there is no hydrocarbon molecule inside the solid supercell, which was cut from its adjacent domains of the simulated unit cell, as presented in Figure 3-1b. This MD simulation setting can be viewed as the synthetic oil in the grain boundaries entering the β -zeolite grain structures. In this regard, the adsorption of the oil inside the boundaries is presumably

negligible. The MD simulation run in the canonical NVT ensemble was performed at 298 K and at the time step of 1fs for at least 3 ns using the LAMMPS simulator. Accordingly, the number of atoms (N), temperature (T), and simulated volume (V) are kept unchanged during the simulation. The temperature was fixed by the Langevin thermostat. The periodic boundary condition and the cut-off distance of 10 Å for non-bonded interaction potentials are also applied during the simulation.

For the clear vision of hydrocarbons accessible to pores in the β -zeolite structure, the solid domain containing adsorbed hydrocarbons was extracted from the adjacent domains and is presented in Figure 3.1c, which depicts the MD snapshot after 3ns run. From this Figure, it is very interesting to observe that there is a single ADA molecule (colored in purple) enters the supercell compared to the other hydrocarbons (BAL and ALK), indicating molecular sieving phenomena to exclude the ADA molecules from the β -zeolite structure while facilitating the adsorption of the latter hydrocarbons. For further elucidation of the observed molecular sieving effect, the MD simulations were subsequently carried out at 298 K for adsorption kinetics of the pure hydrocarbons (ADA, BAL, and ALK) inside the β -zeolite model. The simulated MD conditions are similar to the aforementioned ones. Figures 3.2a, 3.2c, and 3.2e show in turns the MD initial configurations of ADA (3 molecules), BZN (1062 molecules), and ALK (968 molecules) inside the β -zeolite model. The MD simulations were run for durations of 5-8 ns. Self-diffusion coefficient D_s of the hydrocarbon adsorbate is determined by the slope of the plot which describes the linear mean square displacement (MSD) relationship with time, as presented in detail in the subsection 2.3 and in Figures 3.3a, and 3.3b. In addition, the error of the simulated self-diffusivity is estimated using the method published by authors R. Chitra and S. Yashonath⁴³.

Table 3.1: Self-diffusivity of pure hydrocarbons in β -zeolite

Hydrocarbon	D_s (10^{-8} m ² /s)	Error
ALK	1.18	0.18
BZN	0.20	0.06

Table 3.2: Molecular compositions and fractions in β -zeolite

BEA_synthetic_oil	Before	After	Molecular percentage (%)
ADA	369	1	0.87
BAL	393	89	72.96
BZN	394	32	26.17
Total	1156	122	100
BEA_adamantane	3	0	
BEA_alkane	968	116	
BEA_benzene	1062	281	

From Figures 3.3a and 3.3b, it can be clearly seen that values of self-diffusivity of BZN and ALK adsorbates in the β -zeolite model are proportional to 10^{-8} - 10^{-9} m²/s, as shown in Table 3.1, which are commonly observed for light hydrocarbons in the zeolite material, indicating no pore accessible problem of these hydrocarbons to the β -zeolite structure. On the contrary, the MD simulation of pure ADA in the β -zeolite model fails after the first few time

steps due to the excessively high adsorption energy which causes very unstable ADA adsorbate molecules. In addition, the MD simulation of ADA inside the β -zeolite model proceeded at 700 K has found a similar result, indicating that the high kinetic energy of the adsorbate molecules could not overcome the energy barrier induced by the molecular restriction of pores in the solid structure. In this regard, the above MD simulation results confirm the molecular sieving to exclude ADA from the β -zeolite structure model while accommodating the adsorption of the other hydrocarbons (BZN and ALK). For the fact that ADA is the smallest member of the diamondoid family, similar molecular sieving to exclude the larger diamondoids is also expected to occur. From this stage, an interesting question arises how are these MD simulation results utilized to explain experimental observation of the separation of lower diamondoids from oil by β -zeolite and its heat-treated version in the previous work²¹?

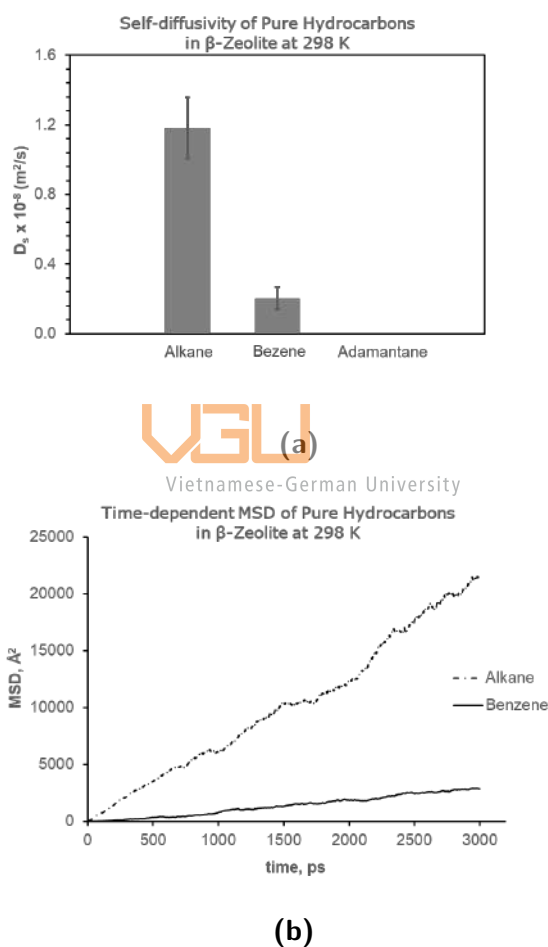


Figure 3.3: Adsorption dynamics analysis in β -zeolite. (a) Self-diffusivity of pure hydrocarbons in β -Zeolite at 298 K. (b) Time-dependent MSD of pure hydrocarbons in β -Zeolite at 298 K.

For the fact that the molecular sieving has been found to exclude the diamondoids from β -zeolite, it is also deduced that there is a similar molecular sieving to preclude the adsorption of cyclic alkanes present predominantly in the light oil fraction including naphthalene, xylenes, phenanthrene, bicyclic, tricyclic compounds and their alkyl derivatives. In other words, the virgin β -zeolite eliminates both isoalkanes and diamondoids. The former species are predominant over the latter in the light oil fraction. Hence, there was a poor separation of diamondoids from oil by the virgin β -zeolite, which has been experimentally observed in our previous work²¹. On the other hand, the heat-treated version of the virgin β -zeolite at 500°C.

for a prolonged period of at least 24 hours leads to partial elimination of aluminum atoms from the virgin zeolite structure and so lateral pore widening, which corresponded to a slight shift in pore size of the heat treated β -zeolite compared to that of the virgin version²¹. Such lateral pore widening will essentially facilitate the greater adsorption of two-dimensional molecules such as cyclic alkanes while still eliminating highly symmetrical molecules like the diamondoids. As a consequence, this is well corroborative with the previous experimental observation of the outperformance of the heat treated β -zeolite over its virgin one for the separation of the diamondoids from oils²¹.

3.2 Adsorption dynamics of Hydrocarbons in Realistic Structural Model of Activated Carbon Fiber ACF-15

In this subsection, the study of hydrocarbon adsorption dynamics in the highly ordered activated carbon fiber (ACF-15) is carried out. Accordingly, the atomistic model of ACF-15, previously constructed by Hybrid Reverse Monte Carlo (HRMC) simulation technique³⁰, is utilized for the MD simulations of the adsorption dynamics presented in the previous subsection 2.4b. Similar MD conditions as aforementioned are also applied. The first MD simulations are to investigate the pore accessibility of adamantane and its adsorption kinetics to the ACF-15 model at temperatures between 298 K and 448 K. Figure 3.4a shows the initial MD configuration that does not initially contain adamantanes inside the solid but rather 613 ADA molecules surrounding it. As shown in Figure 3.4b, the solid region is taken from the surrounding fluid region. Figure 3.4c presents the snapshot of the MD simulation system at 298 K for 3ns after the solid domain containing adsorbed hydrocarbons was extracted from the adjacent domains. From this figure, it is clearly seen that the adamantane can diffuse in all larger pores of the ACF-15 model except the small pores whose critical size is presumably smaller than the smallest dimension (6.8 Å) of adamantane molecule²⁴. Subsequently, the MD configuration as in the snapshot presented in Figure 3.4c was employed as the MD initial configuration for the MD simulations to study the adsorption kinetic behavior at the four different selected temperatures (298 K, 348 K, 398 K, and 448 K). Particularly, the self-diffusion coefficient D_s is determined from the slope of the linear plot of mean square displacement (MSD) against the MD simulation time, as shown in Figure 3.5. The error of the simulated self-diffusion coefficient is estimated using the aforementioned method. Figures 3.6a and 3.6b display the variation of the self-diffusion coefficient with temperature and that with reciprocal temperature, respectively. The latter plot is used to determine pre-factor D_0 and activation energy E_a by the fit of the MD simulated temperature-dependent data with the Arrhenius equation⁴⁴ given as $D_s = D_0 \exp(-\frac{E_a}{k_B T})$. From these figures, a striking feature is that there exists a crossover or transition temperature near 348K. Accordingly, there is a simultaneous increase in the pre-factor D_0 and activation energy E_a from $2.3 \times 10^{-9} \text{ m}^2/\text{s}$ and 1.8 kJ/mole for lower temperatures than 348K to $9.71 \times 10^{-9} \text{ m}^2/\text{s}$ and 6.0 kJ/mole for higher temperatures than 348 K.

Due to the high melting point of adamantane of 270°C, it can be presumed that the relaxation time τ_0 of adamantane at adsorption sites is much longer than the jumping time between neighboring adsorption sites. In this regard, the pre-factor D_0 is approximately determined as:

$$D_0 = \frac{r_0^2}{4\tau_0} \quad (3.1)$$

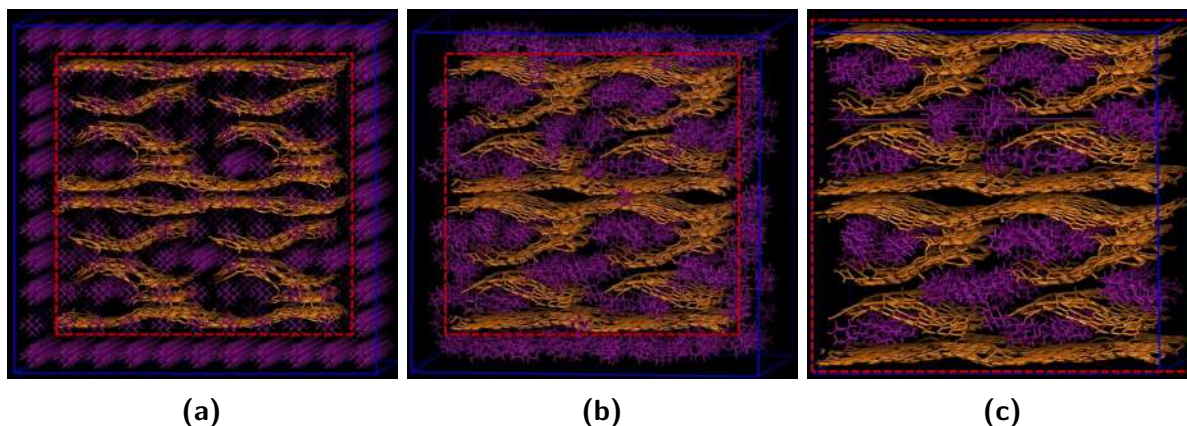


Figure 3.4: Investigation on adsorption accessibility of adamantane to ACF-15. (a) MD initial configuration of adamantane in ACF-15. (b) The configuration of adamantane in ACF-15 after 3ns MD run before taking out the solid. (c) The configuration of adamantane in ACF-15 after 3ns MD run after taking out the solid.

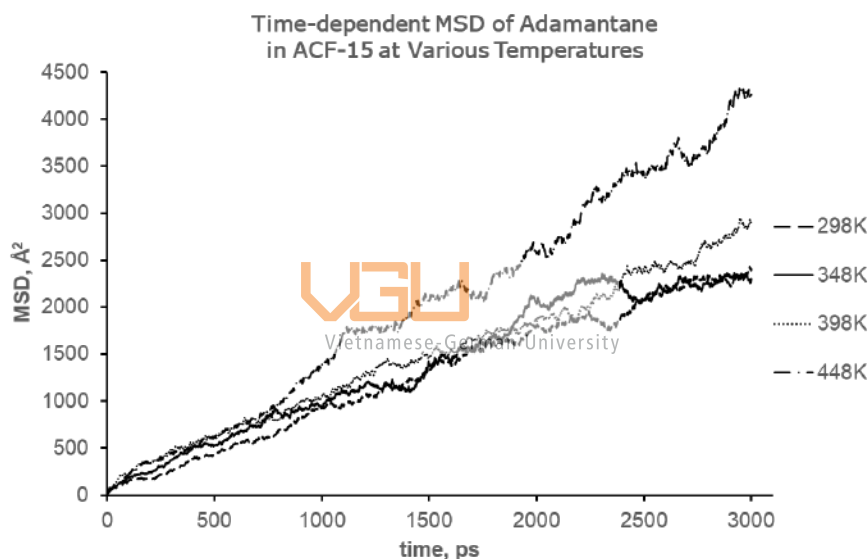


Figure 3.5: Time-dependent MSD of adamantane in ACF-15 at various temperatures.

Table 3.3: Self-diffusivity of adamantane in ACF-15 at various temperature

Adamantane	D_s (10^{-8} m ² /s)	Error
298 K	0.11	0.016
348 K	0.12	0.031
398 K	0.15	0.025
448 K	0.20	0.023

where r_0 is the inter-adsorption site distance.

For the further assumption of temperature independence of r_0 , the relaxation time τ_0 is presumably larger at the lower temperature due to higher adsorption density and lower kinetic energy of the adsorbate, leading to an increase in the pre-factor D_0 with increasing temperature. In practice, it is also noted that the significant difference in the pre-factor D_0 by less than

Table 3.4: Self-diffusivity of pure hydrocarbons in β -zeolite

Temperature	E_a (kJ/mol)	D_0 (10^{-9} m ² /s)
298 – 348 K	1.8	2.3
348 – 448 K	9.71	9.71

an order of magnitude for the same adsorption system measured by different methods is also observed. The increase in the activation energy E_a with increasing temperature arises from the heterogeneity of the adsorption energy landscape. Higher density of the adsorbed phase at lower temperatures than 448 K can be seen from a right shift of peaks in pair distribution functions $g(r)$ between 6.65 Å - 7.35 Å as the temperature rises. As a consequence, the higher density of the adsorbed phase or the high adsorption coverage at the lower temperatures in association with energetically less favored adsorption sites results in lower activation energy to the surface diffusion. This has been experimentally observed^{45,46}.

Table 3.5: Molecular compositions and fractions of hydrocarbons in ACF-15

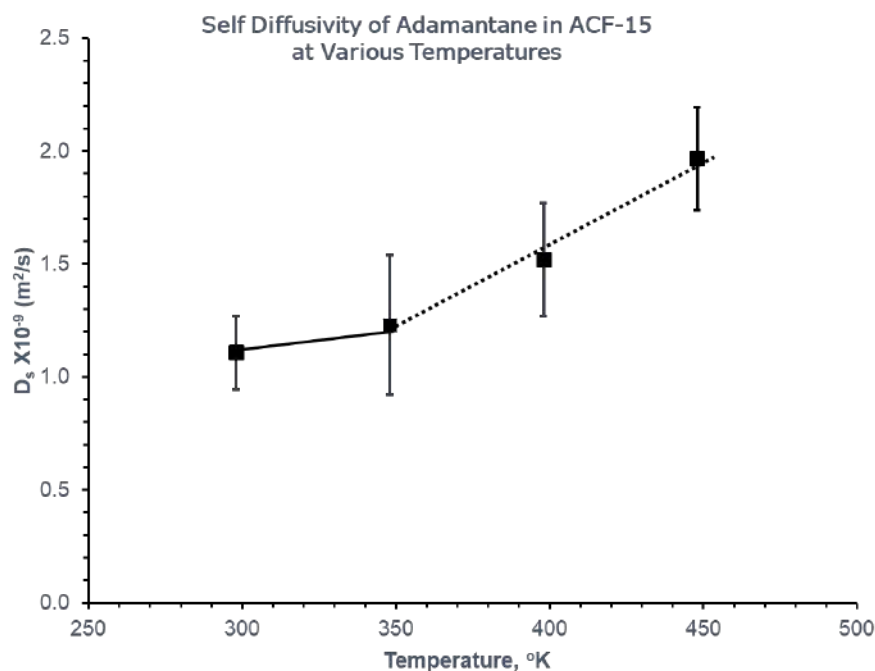
ACF_synthetic_oil	Before	After	Molecular percentage (%)
ADA	278	104	42.43
BAL	274	56	23.18
BZN	277	84	34.39
Total	829	244	100
ACF_adamantane	613	182	
ACF_alkane	475	166	
ACF_benzene	369	232	

Table 3.6: Self-diffusivity of pure hydrocarbons in ACF-15

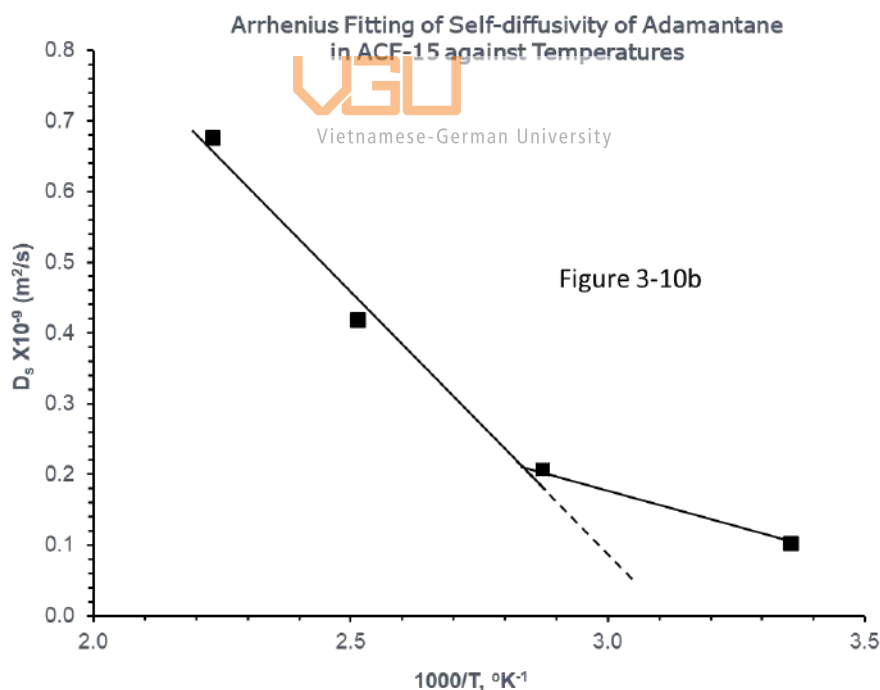
Hydrocarbon	D_s (10^{-8} m ² /s)	Error
ADA	0.11	0.016
BAL	1.26	0.338
BZN	1.38	0.103

From Figure 3.7, it can be foreseen that adamantane molecules are more accessible to the pore system of ACF-15 at lower temperatures than 348 K due to their energetically more favorable self-assembly.

For investigating the capability of ACF-15 to separate diamondoids from crude oil, we further performed the MD simulations of pure BZN and ALK and their mixture at 298 K in the ACF-15 carbon model. Figures 3.8a and 3.8c demonstrate the initial MD configurations of BZN and ALK in the ACF-15 carbon model. The MD snapshot of BZN in the ACF-15 model after a 3ns MD run shows BZN adsorbates access all the pores of the ACF-15 model while excluding ALK adsorbates to the small pores due to the planar geometry of BZN molecule (molecular thickness of 1.4 Å)⁴² compared to much larger kinetic diameter (6.2 Å)⁴⁷ of the ALK adsorbates. For comparing the self-diffusion coefficient among the studied hydrocarbons



(a)



(b)

Figure 3.6: Adsorption dynamics analysis of adamantane in ACF-15. (a) Self-diffusivity of adamantane in ACF-15 at various temperatures. (b) Arrhenius fitting of self-diffusivity of adamantane in ACF-15 against temperatures.

(ADA, BZN, ALK) in the ACF-15 model, the initial MD configurations having (369 molecules) of BZN and (475 molecules) of ALK in the carbon model, are prepared for MD simulations to determine self-diffusivity and its error by the aforementioned method. Figure 3.9 indicates

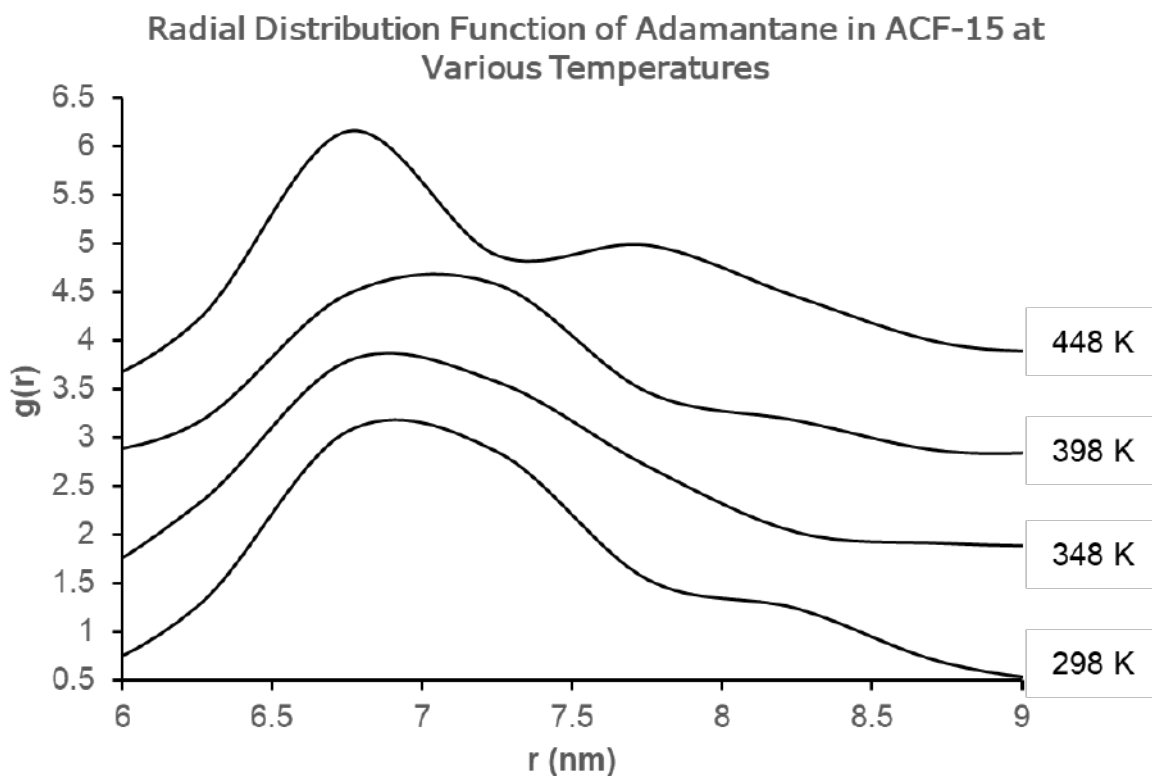


Figure 3.7: Radial distribution function of adamantane in ACF-15 at various temperatures.

the significantly faster diffusion rate of BZN and ALK adsorbates ($10.22 \times 10^{-8} \text{ m}^2/\text{s}$ and $8.38 \times 10^{-8} \text{ m}^2/\text{s}$, respectively) in the ACF-15 model than ADA adsorbates ($3.88 \times 10^{-8} \text{ m}^2/\text{s}$) by a factor. Accordingly, a question is if the higher diffusion rate of the former adsorbates possibly denotes lower activation energy E_a of the adsorbates to access the pore system of the ACF-15 model. In order to render an answer to this question, we proceeded with the MD simulations to study the pore accessibility of the mixture of ADA, BZN, and ALK in the carbon model followed by the determination of the self-diffusion coefficient of the individual adsorbates as their mixture is initially placed inside the pore structure of the ACF-15 model. In particular, the hydrocarbon mixture containing 278 ADA molecules, 277 BZN molecules, and 274 ALK molecules was arranged outside the unit cell of the ACF-15 model to create the unit cell of the initial MD configuration, as shown in Figure 3.10a.

Table 3.7: Self-diffusivity of pure hydrocarbons in ACF-15

Hydrocarbon	$D_s \times 10^{-8} \text{ (m}^2/\text{s)}$	Error
ACF_ALK_298K	0.08	0.014
ACF_BZN_298K	0.10	0.026
ACF_ADA_298K	0.11	0.005
ACF_ALK_448K	0.16	0.057
ACF_BZN_448K	0.21	0.053
ACF_ADA_448K	0.25	0.011

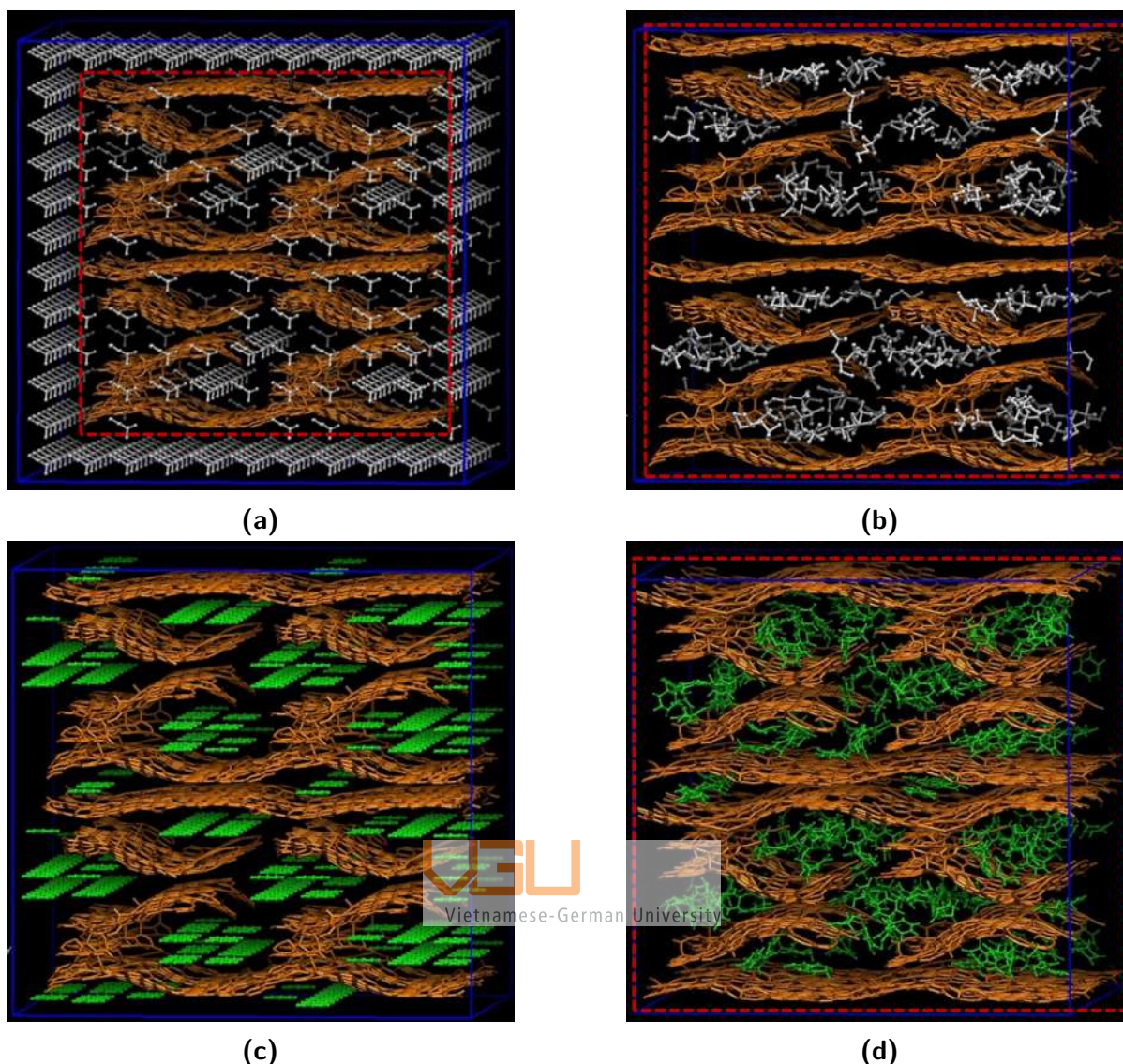


Figure 3.8: Investigation on adsorption accessibility of pure hydrocarbons to ACF-15 adsorbent. (a) MD Initial configuration of alkane in ACF-15. (b) MD snapshot of alkane in ACF-15. (c) MD Initial configuration of benzene in ACF-15. (d) MD snapshot of benzene in ACF-15.

For this arrangement, the hydrocarbon mixture is assumed to enter the pore system of the ACF-15 model from the bulk phase dwelling inside grain boundary domains. Figure 3.10b presents the MD snapshot of the adsorbed phase inside the carbon model after the 5 ns MD run. From Figure 3.10, it is interesting to see that the adsorbed phase contains a slightly high number of ADA adsorbates (104 molecules) compared to that of BZN (84 molecules) and ALK (56 molecules), indicating comparable or even lower activation energy E_a of the former adsorbate to access the pore structure of the ACF-15 model. To have a better understanding of the competitive adsorption kinetics among the hydrocarbons, the initial MD configuration is constructed from the adsorbed phase and the carbon model only, as shown in Figure 3.10c. The comparison in self-diffusion coefficient among the hydrocarbons of the adsorbed phase inside the carbon model, as shown in Figures 3.12a and 3.12b, indicates the faster diffusion rate $1.1 \times 10^{-9} \text{ m}^2/\text{s}$ of ADA adsorbate than that of ALK ($0.8 \times 10^{-9} \text{ m}^2/\text{s}$) adsorbate and that of BZN ($1.0 \times 10^{-9} \text{ m}^2/\text{s}$) adsorbate. This seems to be contradictory to the significantly faster diffusion rate of ALK than ADA observed in the case of the single adsorption dynamics

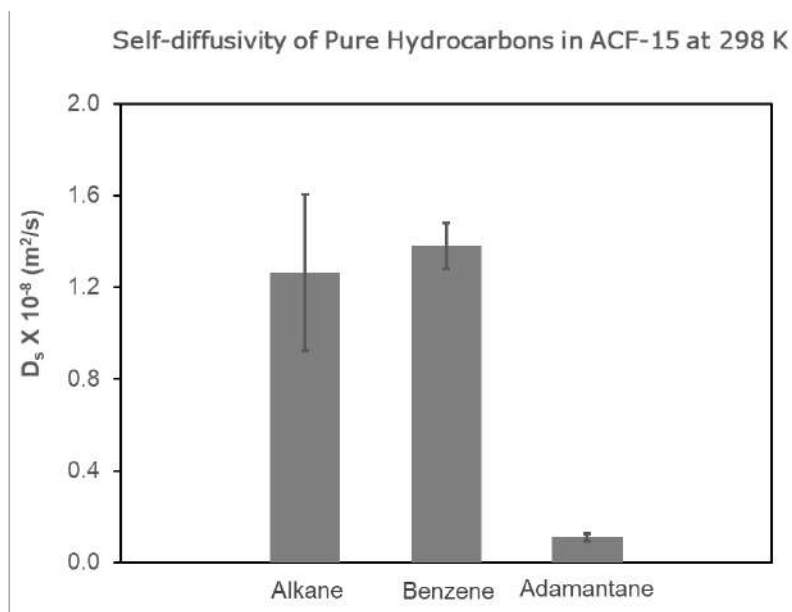


Figure 3.9: Self-diffusivity of pure hydrocarbons in ACF-15 at 298 K.

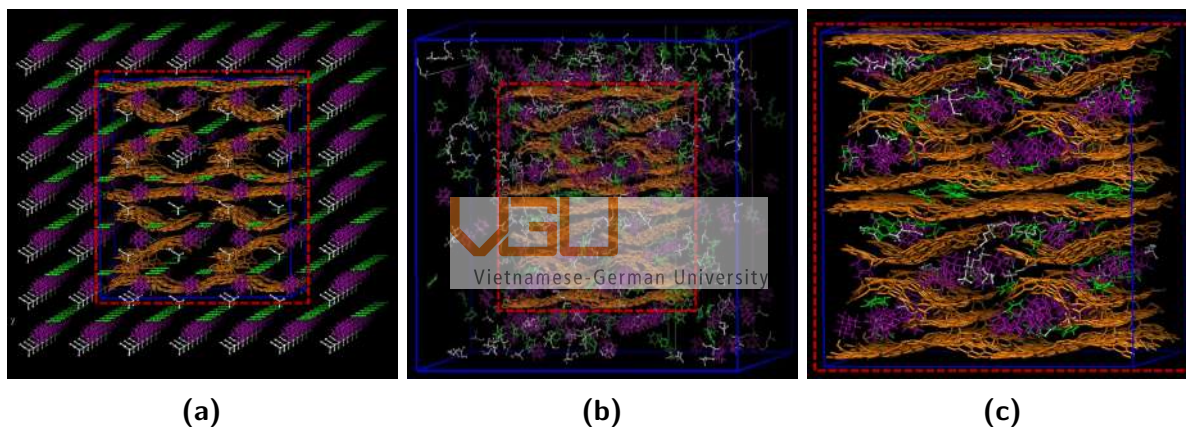


Figure 3.10: Investigation on adsorption accessibility of synthetic oil to ACF-15. (a) MD initial configuration of synthetic oil in ACF-15. (b) The configuration of synthetic oil in ACF-15 after 3ns MD run before taking out the solid. (c) The configuration of synthetic oil in ACF-15 after 3ns MD run after taking out the solid.

of the same hydrocarbons. The self-assembly of ADA, a symmetrical and rigid molecule, is energetically more favorable than ALK, an unsymmetrical and flexible molecule⁴⁸, especially under confinement conditions. As a consequence, the adsorbed phase of ADA is expected to be denser than that of ALK, indicating the lower activation energy E_a of the former adsorbate. From the above presentation, despite energetically more favorable adsorption of ADA compared to ALK in ACF-15, the sufficiently good separation of ADA from the hydrocarbon mixture (ADA, BZN, ALK) is not practically expected, especially a tiny concentration of diamondoids in crude oils and extractable organic matter (EOM). However, it is very interesting to be deduced that the lower activation energy E_a of ADA relative to that of ALK might be related to the self-assembly under the confinement. As a consequence, a question arises is if there exists an optimum pore size that significantly enhances the self-assembly or the adsorption coverage of ADA adsorbate to that of BZN and ALK in the case of the competitive adsorption of the mixture of these hydrocarbons.

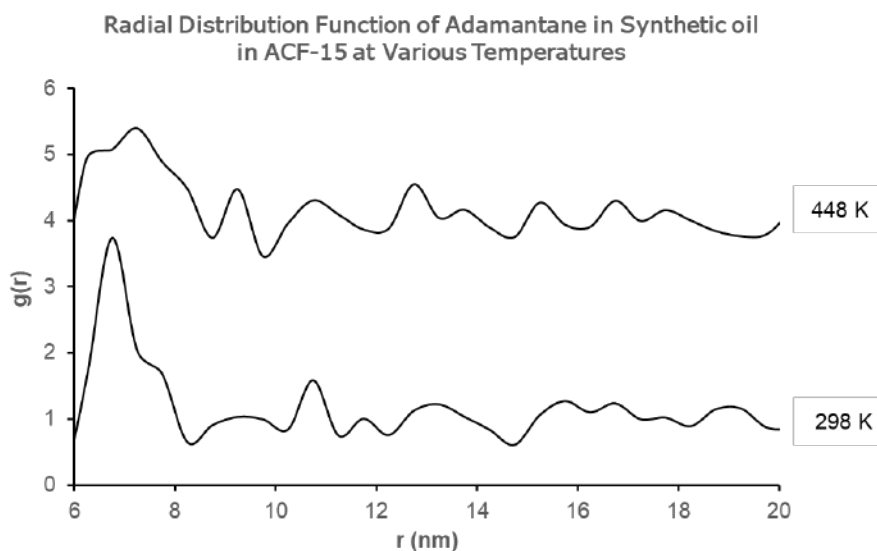
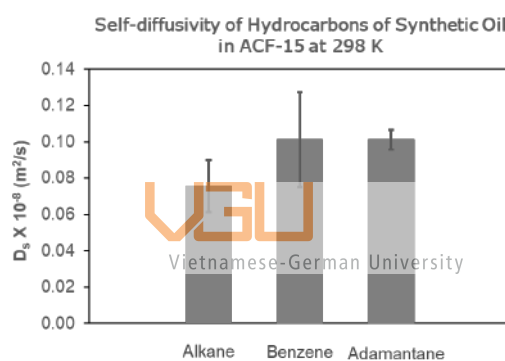
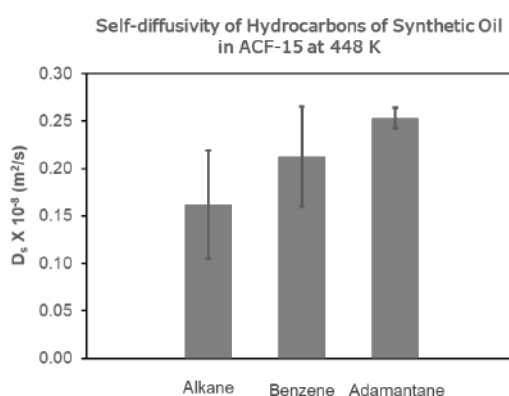


Figure 3.11: Radial distribution function of adamantane in synthetic oil in ACF-15 at various temperatures.



(a)



(b)

Figure 3.12: Adsorption dynamics analysis of adamantane in ACF-15. (a) Self-diffusivity of hydrocarbons of synthetic oil in ACF-15 at various temperatures. (b) Self-diffusivity of hydrocarbons of synthetic oil in ACF-15 against temperatures.

3.3 Adsorption dynamics of Hydrocarbons in Graphitic Slit-Like Pore

In this subsection, we investigate the pore accessibility of single hydrocarbon components (ADA, BZN, and ALK) in graphitic slit-like pores (GRP) as illustrated in Figures 3.13, 3.14, and 3.15. The slit-like pore model consists of two identical opposite walls, each containing two graphene layers which approximately generate the adsorption field strength of the infinite thickness graphitic wall. Figures 3.13a, 3.14a, and 3.15a show all the initial MD configurations which do not initially include adsorbates inside pores. Similar MD conditions as aforementioned are also applied.

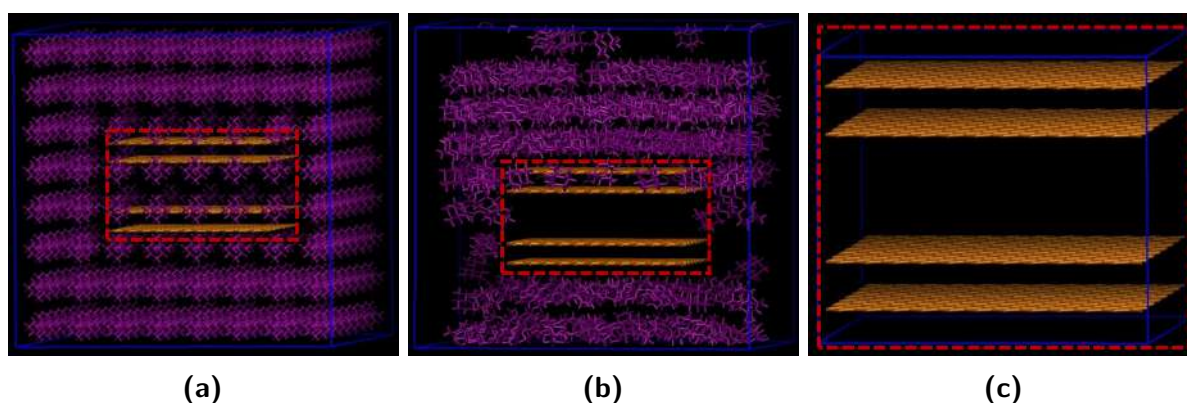


Figure 3.13: Investigation on adsorption accessibility of adamantane to 5.5 Å graphitic slit pore. (a) MD initial configuration of adamantane in graphitic slit pore. (b) The configuration of adamantane in graphitic slit pore after 3ns MD run. (c) MD initial configuration has no adamantane in graphitic slit pore after 3ns MD run.

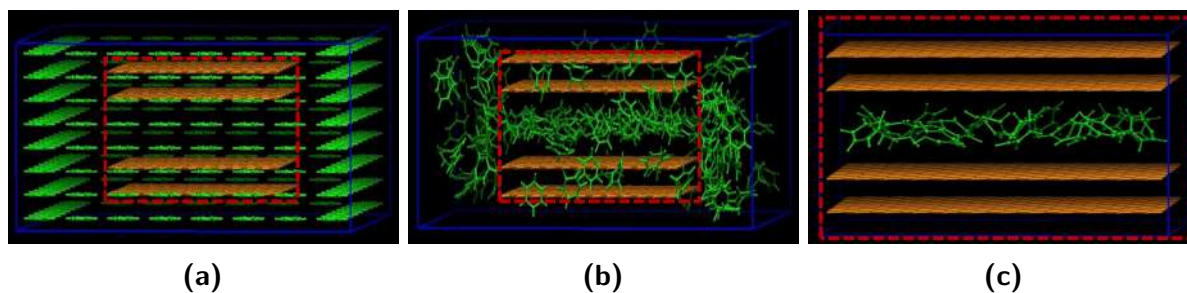


Figure 3.14: Investigation on adsorption accessibility of benzene to 5.5 Å graphitic slit pore. (a) MD initial configuration of benzene in graphitic slit pore. (b) The configuration of benzene in graphitic slit pore after 3ns MD run. (c) The configuration of benzene in graphitic slit pore of 3ns MD run after taking out the solid.

Figure 3.16 presenting snapshots after 3ns MD runs indicate the onset of the molecular sieving that occurs for the internal pore size of 5.5 Å to exclude ADA adsorbates while accommodating BZN and ALK adsorbates to enter the pore. On the contrary, all the studied hydrocarbons are accommodated to enter larger pores whose internal width is greater than 6 Å. This is consistent with the molecular dimensions of ADA, BZN, and ALK adsorbates of 6.8 Å, 5.85 Å, and 6.2 Å, respectively. From the MD snapshots of the hydrocarbon mixture adsorption dynamics, we determined molecular fractions of the adsorbed hydrocarbons in all the larger pores whose internal pore widths are 6.0 Å, 9.0 Å, 12 Å, and 15 Å, as presented in Table 3.8 and Figures 3.17, 3.18, 3.19 and 3.20. Accordingly, it is very interesting to observe

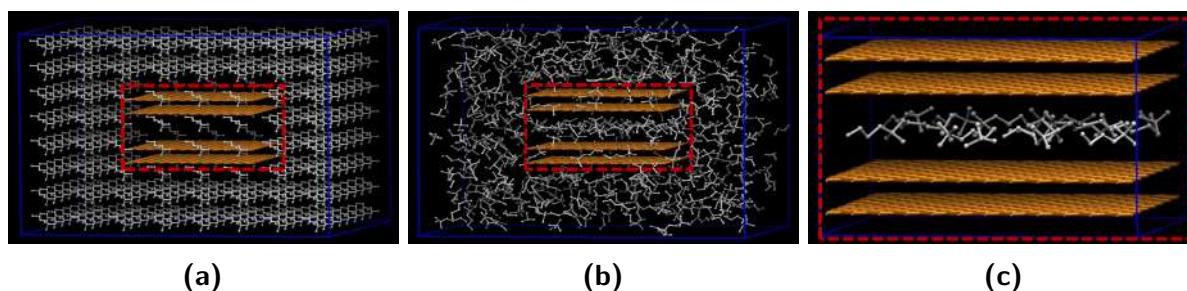


Figure 3.15: Investigation on adsorption accessibility of alkane to 5.5 Å graphitic slit pore. (a) MD initial configuration of alkane in graphitic slit pore. (b) The configuration of alkane in graphitic slit pore after 3ns MD run. (c) The configuration of alkane in graphitic slit pore of 3ns MD run after taking out the solid.

that the highest molecular fraction of ADA adsorbates over that of BZN and ALK occurs in the pore of 12 Å. It is noted that the initial molecular compositions of ADA, BZN, and ALK are almost equal in all the initial MD simulations, as presented in Table 3.8. As a consequence, there exists the optimal pore size in the adjacent pore size domain of 12 Å, as depicted in Figure 3.24. A closer look at the molecular packing configuration of the adsorbed layers inside the larger pores than 5.5 Å, as presented in Figure 3.21, reveals that the adsorbed ADA phase in the pore size of 12 Å contains exactly two adsorbed layers near two opposite walls of the studied pore where the location of the adsorption energy wells is as expected⁴⁸. Hence, the adsorption field by the two graphitic pore walls highly stabilizes the self-assembly of ADA inside the pore which subsequently gives rise to the high adsorption coverage. Meanwhile, the adsorbed phases in the pores (6 Å, 9 Å, and 15 Å) contain either less than 1.5 layers or larger than 2 layers which do not entirely fall within the domain of the adsorption wells, leading to much weaker stabilization of the self-assembly of ADA adsorbates in these non-optimal pores or much lower adsorption coverage. This observation could arise from the enhanced entropy of the ADA molecule by its rigidity and symmetry of this molecule⁴⁸. Such entropic enhancement essentially results in energetically more favorable self-assembly of ADA adsorbates compared to BZN and ALK under the confinement which is indicative of preferential ADA adsorption in all the studied pores (6 Å, 9 Å, 12 Å, 15 Å). In particular, a small pore of 6 Å has a single adsorption potential well that is possibly stronger for ALK and BZN adsorbates and could be counterbalanced by the higher entropy of ADA adsorbate, leading the preferential ADA adsorption⁴⁸. It is also deduced that there will be less difference in the adsorption enthalpy between the studied hydrocarbons in larger pores (9 Å, 12 Å), which accommodates up to two adsorbed layers while maintaining the entropic difference. As a result, the predominant ADA adsorption in the pore of 12 Å having the double well adsorption potential is observed, as presented in Figure 3.20 and Table 3.8. For the wider pore (15 Å) whose two adsorption potential wells are well separated by at least one adsorbed layer, the centered adsorption well depth increases, possibly denoting an increase in the adsorption enthalpy difference between the studied hydrocarbons, which eventually induces the significant reduction in the preferential ADA adsorption degree. Furthermore, the pair distribution functions of the ADA adsorbed phase in the investigated pores (6 Å), as illustrated in Figure 3.22, evidently show the largest number of the nearest neighbors of ADA around the centered ADA molecule (represented by peak a), denoting closest packing and uniformity of the self-assembly of ADA adsorbed phase in the pore of 12 Å.

The determination of the self-diffusion coefficients D_s of ADA, BZN, and ALK in their adsorbed mixtures in the graphitic slit pores of 5.5 - 15 Å shows the fastest diffusion rate of

Table 3.8: Molecular compositions and fractions of hydrocarbons of synthetic oil in graphitic slit pore at various pore sizes

GRP5.5	Before	After	Percentage
ADA	120	0	0.0
ALK	117	9	64.29
BZN	117	5	35.71
Total	354	14	100.0
GRP6			
ADA	118	7	40.97
ALK	117	4	23.61
BZN	117	6	35.42
Total	352	17	100.0
GRP9			
ADA	107	21	44.68
ALK	107	13	27.66
BZN	107	13	27.66
Total	321	47	100.0
GRP12			
ADA	107	61	77.07
ALK	107	8	10.11
BZN	116	11	12.82
Total	330	80	100.0
GRP15			
ADA	107	36	46.22
ALK	114	23	27.72
BZN	116	22	26.06
Total	337	81	100.0

ADA in all the studied pores, as presented in Table 3.9 and Figure 3.23. It is further observed that the ratio of the self-diffusion coefficient of ADA to that of ALK or kinetic selectivity of ADA to ALK reaches the largest value of nearly 10 in the pore of 12 Å but at best 3 in the remaining pores, as shown in Figure 3.23. These results are very consistent with the most ADA abundance of 76% in the pore 12 Å and so the highest adsorption selectivity of ADA over the other hydrocarbons (BZN and ALK). The highest diffusion rate of ADA in the pore of 12 Å arises from the stability of the self-assembly of ADA in the pore that essentially reduces the activation energy for the diffusion of ADA into the pore in comparison with that of the remaining hydrocarbons, as aforementioned. Finally, the temperature effect on the kinetic selectivity of ADA to BZN and ALK in the pore of 12 Å is also investigated in this thesis. In particular, the self-diffusion coefficients of ADA, BZN, and ADA are estimated from the MD simulations of their mixture at a higher temperature of 700 K, as presented in Figure 3.25.

Table 3.9: Self-diffusivity of hydrocarbons of synthetic oil in GRP at various temperatures

Hydrocarbon	D_s (10^{-8} m ² /s)	Error
GRP6.0_BAL	1.82	1.011
GRP6.0_BZN	3.21	2.145
GRP6.0_ADA	3.14	2.931
GRP9.0_BAL	1.23	0.288
GRP9.0_BZN	2.52	0.034
GRP9.0_ADA	3.40	0.560
GRP12.0_BAL	0.19	0.080
GRP12.0_BZN	0.47	0.014
GRP12.0_ADA	1.73	0.729
GRP15.0_BAL	2.44	1.866
GRP15.0_BZN	3.52	1.171
GRP15.0_ADA	5.58	2.618

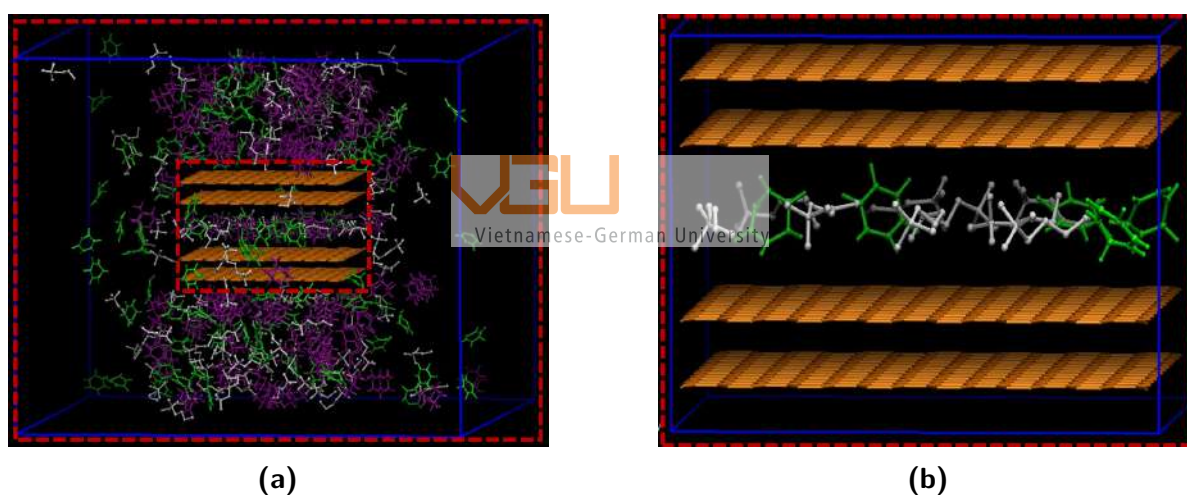


Figure 3.16: Investigation on adsorption accessibility of the synthetic oil to 5.5 Å graphitic slit pore. (a) MD initial configuration of the synthetic oil in 5.5 Å graphitic slit pore. (b) MD snapshot indicates molecular sieving excluding adamantane from the pore size of 5.5 Å.

From this figure, it can be observed that the kinetic selectivity of ADA over ALK reduces to near unity, indicating the strong temperature impact on the stability of the self-assembly of the adsorbed ADA that raises significantly the activation energy for the ADA diffusion into the pore. The stability of the self-assembly can be seen through a shift of the first nearest neighbor peak at 700 K compared to that of 298 K, indicating a significant reduction in the number of the nearest neighbors at the high temperature, as demonstrated in Figure 3.26.

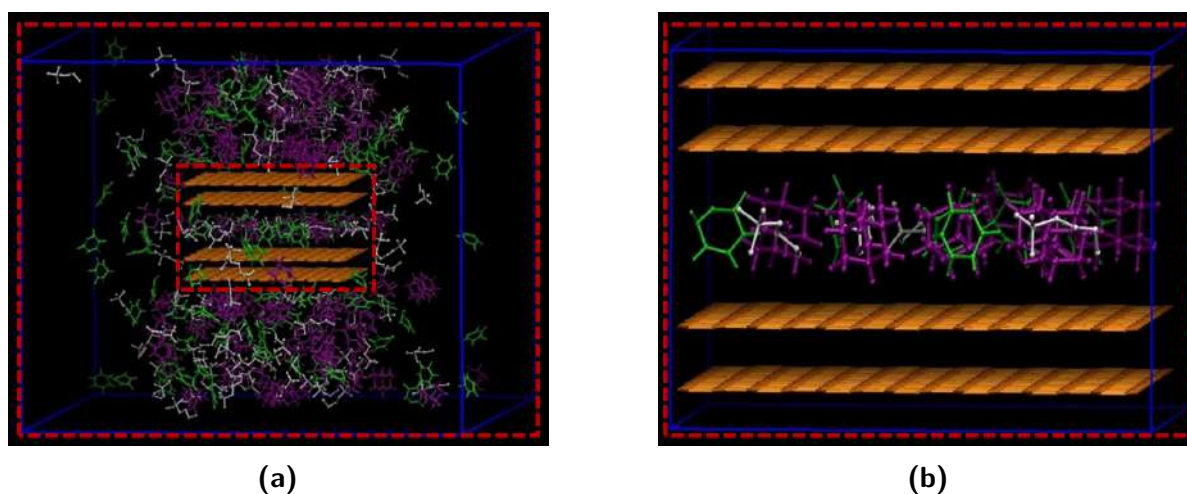


Figure 3.17: Investigation on adsorption accessibility of the synthetic oil to 6 Å graphitic slit pore. (a) MD initial configuration of the synthetic oil in 6 Å graphitic slit pore. (b) MD snapshot of synthetic oil in 6 Å graphitic slit pore of 3ns MD run after taking out the solid.

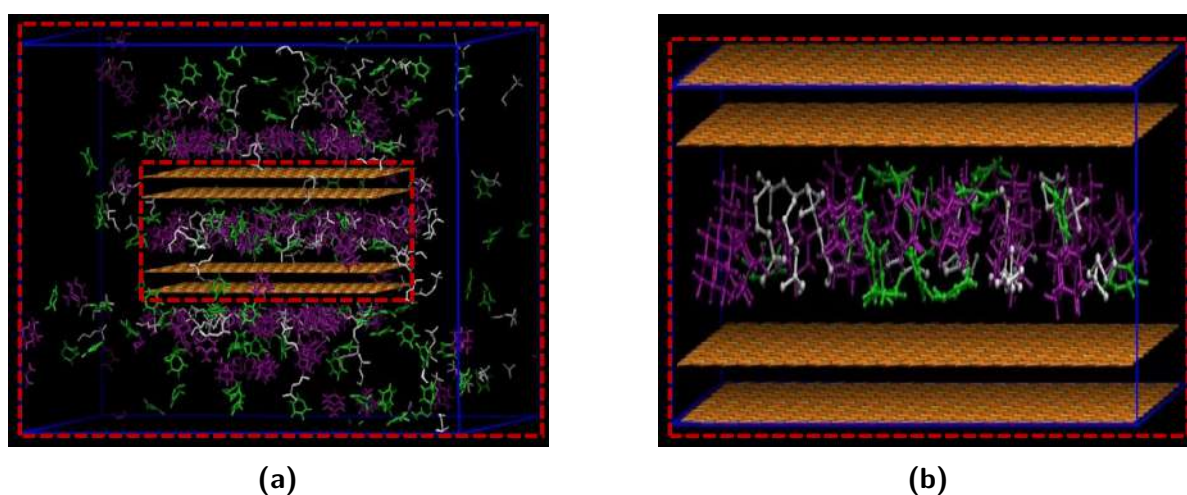


Figure 3.18: Investigation on adsorption accessibility of the synthetic oil to 9 Å graphitic slit pore. (a) MD initial configuration of the synthetic oil in 9 Å graphitic slit pore. (b) MD snapshot of synthetic oil in 9 Å graphitic slit pore of 5ns MD run after taking out the solid.

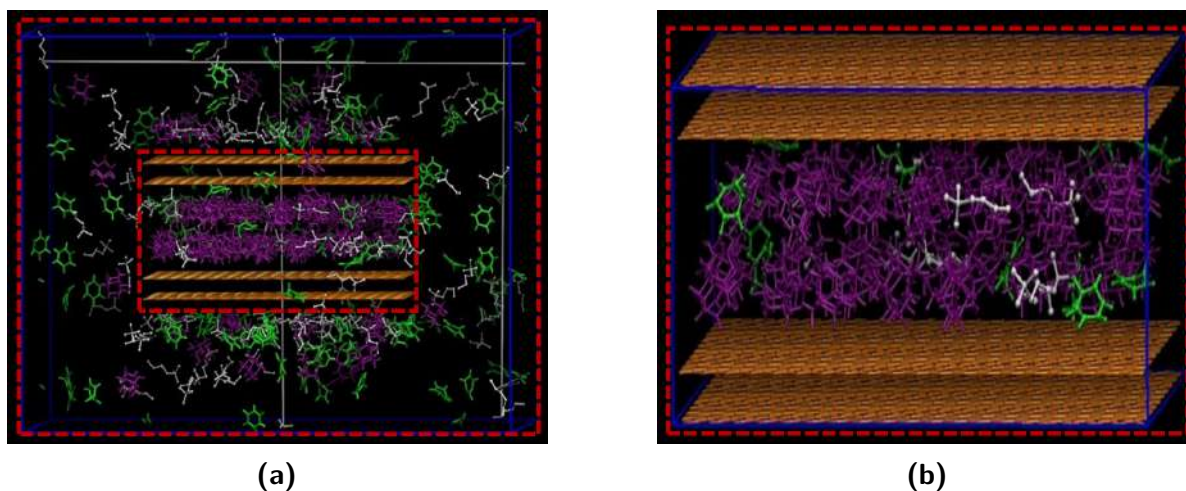


Figure 3.19: Investigation on adsorption accessibility of the synthetic oil to 12 Å graphitic slit pore. (a) MD initial configuration of the synthetic oil in 12 Å graphitic slit pore. (b) MD snapshot of synthetic oil in 12 Å graphitic slit pore of 5ns MD run after taking out the solid.

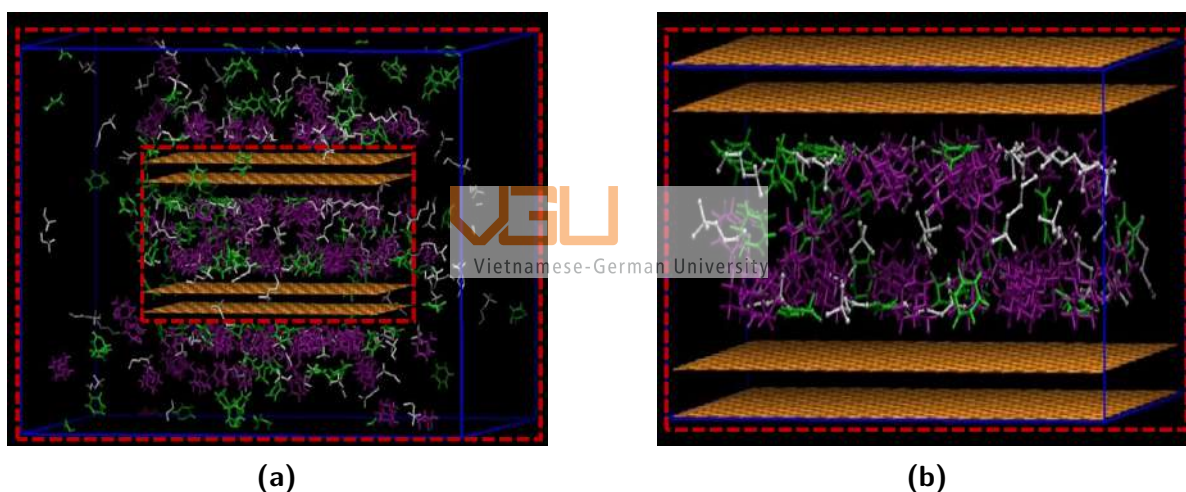


Figure 3.20: Investigation on adsorption accessibility of the synthetic oil to 15 Å graphitic slit pore. (a) MD initial configuration of the synthetic oil in 15 Å graphitic slit pore. (b) MD snapshot of synthetic oil in 15 Å graphitic slit pore of 5ns MD run after taking out the solid.

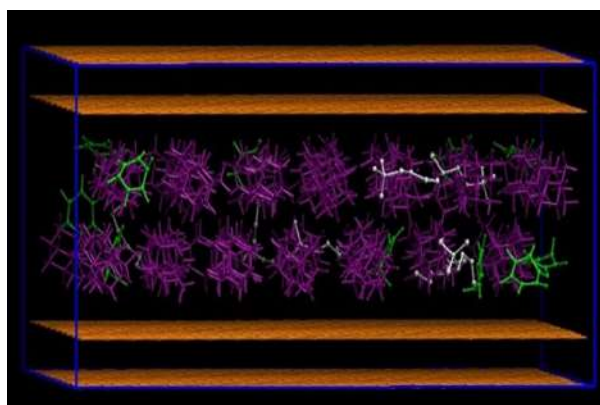


Figure 3.21: Molecular packing configuration in the pore size of 12 Å

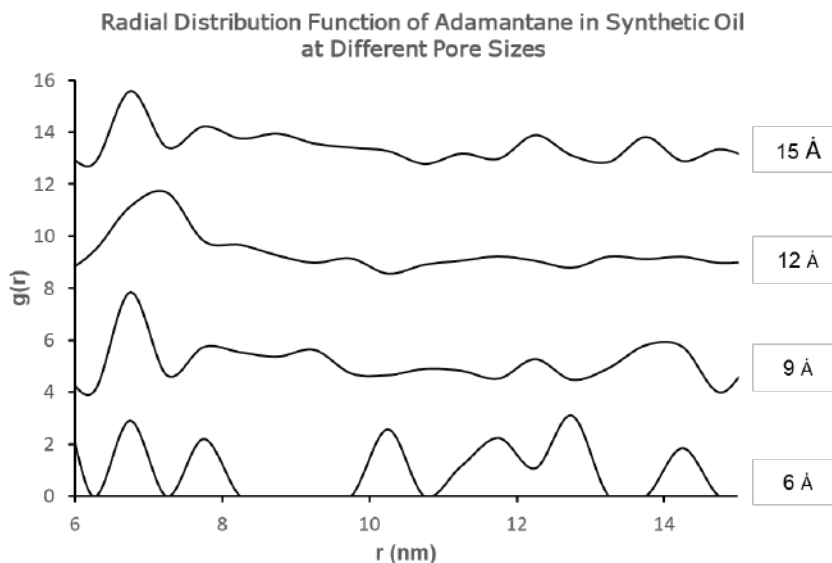


Figure 3.22: Radial distribution function of adamantane in synthetic oil at different pore sizes

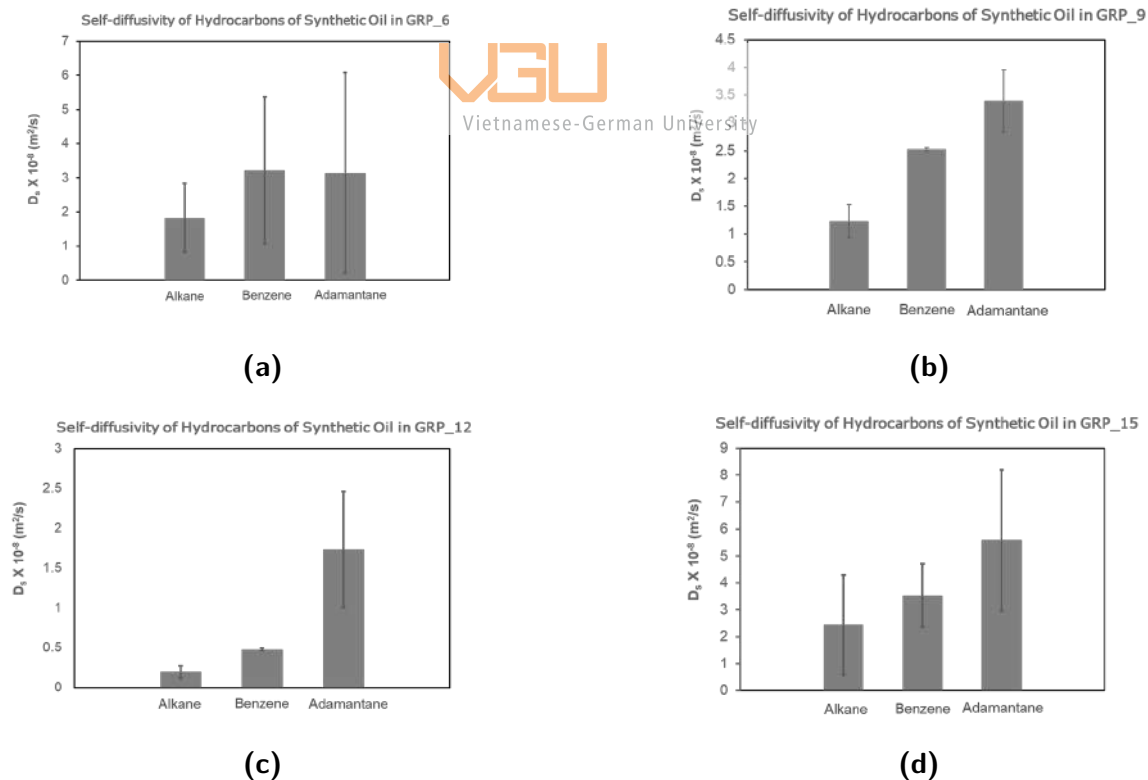


Figure 3.23: Adamantane adsorption dynamics analysis in graphitic slit pore at different pore sizes. (a) Self-diffusivity of hydrocarbons of synthetic oil in 6 Å graphitic slit pore. (b) Self-diffusivity of hydrocarbons of synthetic oil in 9 Å graphitic slit pore. (c) Self-diffusivity of hydrocarbons of synthetic oil in 12 Å graphitic slit pore. (d) Self-diffusivity of hydrocarbons of synthetic oil in 15 Å graphitic slit pore.

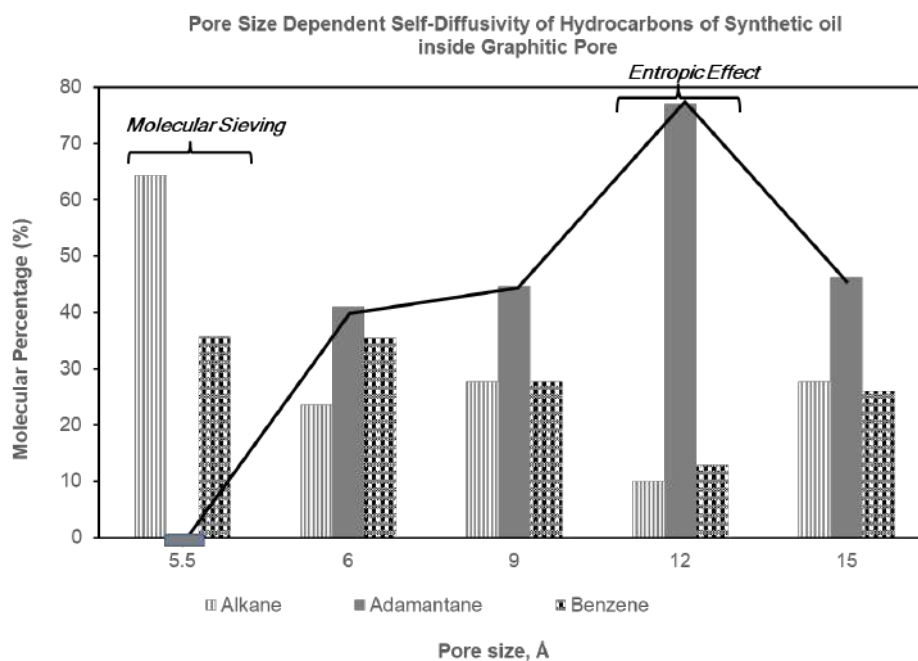


Figure 3.24: Self-diffusivity of hydrocarbons of synthetic oil in graphitic slit pore at different pore sizes

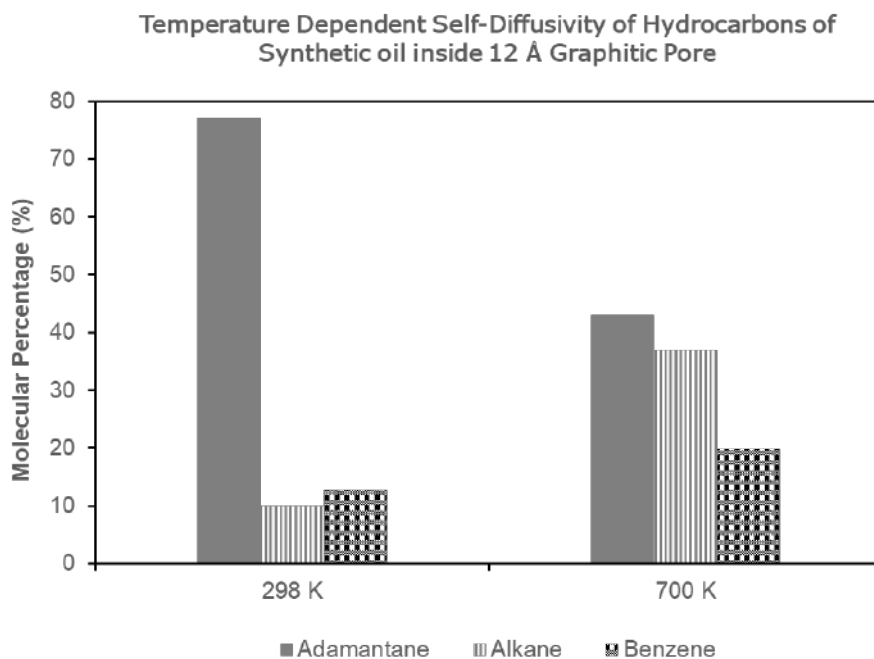


Figure 3.25: Self-diffusivity of hydrocarbons of synthetic oil in 12 Å graphitic pore at different temperatures

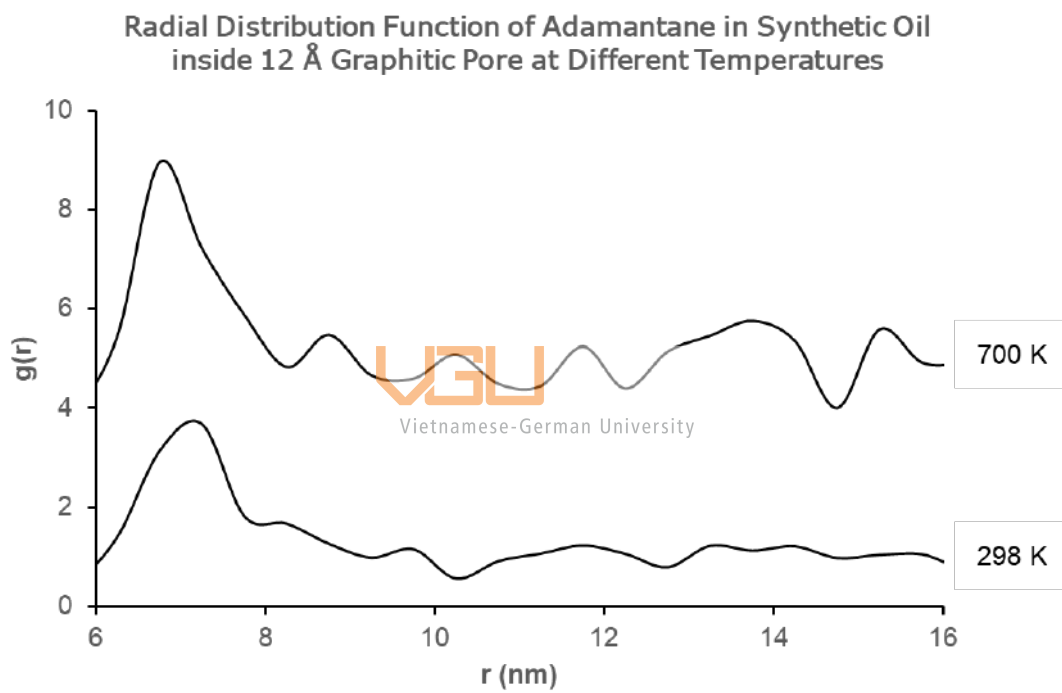


Figure 3.26: Radial distribution function of adamantane in synthetic oil inside 12 Å graphitic pore at different temperatures

Conclusions

In this thesis, the molecular dynamics (MD) simulation method is mainly used to investigate the single and mixture adsorption dynamics of the hydrocarbons (ADA, BZN, ALK) in several microporous adsorbent models including β -zeolite, activated carbon ACF-15, and graphitic slit-like pores. For β -zeolite, the molecular sieving (MS) phenomena have been found to exclude the ADA adsorbates while permitting the BZN and ALK adsorbates to enter the pore system. The latter hydrocarbons tentatively represent alkanes and aromatic compounds in light oil fractions, respectively. Hence, the mixture of the hydrocarbons (ADA, BZN, ALK) is presumably considered synthetic oil. The molecular sieving is well corroborative with the enrichment in lower-diamondoids in N_2 effluent from the bed of virgin β -zeolite and its heat-treated version, as experimentally observed in the previous work²¹. Thus, the pore-widening heat treatment further enhances the non-diamondoid uptake in the heat-treated version of β -zeolite, leading to better separation of lower diamondoids from crude oil, as previously reported²¹.

For the adsorption dynamics in activated carbon fiber ACF-15 at various temperatures (298 K – 448 K), it has been found that the temperature-dependent self-diffusion coefficients of ADA reveal a transition from low activation energy in the low-temperature range (298 K – 348 K) to the higher activation energy for the higher temperature range (348 K – 448 K) as the self-diffusivity data are fitted to the Arrhenius equation. This denotes the strong entropic effect that essentially facilitates the low-temperature self-assembly of ADA adsorbates, leading to the preferential adsorption of ADA adsorbates to the other hydrocarbons (BZN, ALK) in the ACF-15 carbon model. However, it can be foreseen that the preferential adsorption uptake of ADA does not suffice to provide a good separation of ADA from oils containing tiny amounts of diamondoids.

For the adsorption dynamics in graphitic slit-like pore models whose internal pore size varies from 5.5 Å to 15 Å, it has been found that the faster diffusion of the hydrocarbons in the graphitic pore model than in the ACF-15 model due to the defect-free former model. It has also been observed that the molecular sieving occurs only for the smallest pore of 5.5 Å that excludes ADA adsorbate while accommodating BZN and ALK, providing further supporting evidence on the pore-widening heat treatment of β -zeolite that maintains the ADA-exclusive molecular sieving phenomena while increasing the non-diamondoid adsorption uptake. Finally, the striking feature has been seen that there exists the optimal pore size accommodating two adsorbed layers of ADA that indicates predominant adsorption uptake of ADA over BZN and ALK. In other words, this potentially offers the effective separation method for the separation

of low ADA concentrations from crude oils or rock extractable organic matter whereby the enriched ADA concentration through the MSC (5.5 Å) follows by trapping diamondoids in the graphitic pore of 12 Å.



References

1. Atkins, P., & Overton, T. (2010). *Shriver and Atkins' inorganic chemistry*. Oxford University Press, USA.
2. Schoell, M., & Carlson, R. M. (1999). Diamondoids and oil are not forever. *Nature*, 399(6731), 15-16.
3. Balaban, A. T., & Schleyer, P. V. R. (1978). Systematic classification and nomenclature of diamond hydrocarbons—I: Graph-theoretical enumeration of polymantanes. *Tetrahedron*, 34(24), 3599-3609.
4. Hernández-Rojas, J., & Calvo, F. (2019). The structure of adamantane clusters: atomistic vs. coarse-grained predictions from global optimization. *Frontiers in Chemistry*, 7, 573.
5. Dahl, J. E., Moldowan, J. M., Peters, K. E., Claypool, G. E., Rooney, M. A., Michael, G. E., ... & Kohnen, M. L. (1999). Diamondoid hydrocarbons as indicators of natural oil cracking. *Nature*, 399(6731), 54-57.
6. Nasir, S., & Fazeelat, T. (2013). Diamondoid hydrocarbons as maturity indicators for condensates from southern Indus Basin, Pakistan. *Journal of Chemistry*, 2013.
7. Mansuy, L., Philp, R. P., & Allen, J. (1997). Source identification of oil spills based on the isotopic composition of individual components in weathered oil samples. *Environmental Science & Technology*, 31(12), 3417-3425.
8. Lengger, S. K., Scarlett, A. G., West, C. E., & Rowland, S. J. (2013). Diamondoid diacids ('O4' species) in oil sands process-affected water. *Rapid Communications in Mass Spectrometry*, 27(23), 2648-2654.
9. Rander, T., Bischoff, T., Knecht, A., Wolter, D., Richter, R., Merli, A., & Möller, T. (2017). Electronic and optical properties of methylated adamantanes. *Journal of the American Chemical Society*, 139(32), 11132-11137.
10. Harvey, B. G., Harrison, K. W., Davis, M. C., Chafin, A. P., Baca, J., & Merriman, W. W. (2016). Molecular design and characterization of high-cetane alkyl diamondoid fuels. *Energy & Fuels*, 30(12), 10171-10178.

-
11. Morcombe, C. R., & Zilm, K. W. (2003). Chemical shift referencing in MAS solid state NMR. *Journal of Magnetic Resonance*, *162*(2), 479-486.
 12. Maugh, T. H. (1979). Panel Urges Wide Use of Antiviral Drug: NIH group says amantadine should be used for both prevention and therapy of influenza A in the next epidemic. *Science*, *206*(4422), 1058-1060.
 13. Sonnberg, L. (2003). *The Complete Pill Guide: Everything You Need to Know about Generic and Brand-Name Prescription Drugs*. Barnes & Noble.
 14. Boukrinskaia, A. G., Serbin, A. V., Bogdan, O. P., Stotskaya, L. L., Alymova, I. V., & Klimochkin, Y. N. (1999). *U.S. Patent No. 5,880,154*. Washington, DC: U.S. Patent and Trademark Office.
 15. Prelog, V., & Seiwert, R. (1941). Über die synthese des adamantans. *Berichte der deutschen chemischen Gesellschaft (A and B Series)*, *74*(10), 1644-1648.
 16. Nakahara, S., Stauss, S., Kato, T., Sasaki, T., & Terashima, K. (2011). Synthesis of higher diamondoids by pulsed laser ablation plasmas in supercritical CO₂. *Journal of Applied Physics*, *109*(12), 123304.
 17. Nakahara, S., Stauss, S., Miyazoe, H., Shizuno, T., Suzuki, M., Kataoka, H., ... & Terashima, K. (2010). Pulsed laser ablation synthesis of diamond molecules in supercritical fluids. *Applied Physics Express*, *3*(9), 096201.
 18. Bachmann, P. K., Leers, D., & Lydtin, H. (1991). Towards a general concept of diamond chemical vapour deposition. *Diamond and related materials*, *1*(1), 1-12.
 19. Liang, Q., Xiong, Y., Fang, C., & Li, Y. (2012). Quantitative analysis of diamondoids in crude oils using gas chromatography–triple quadrupole mass spectrometry. *Organic Geochemistry*, *43*, 83-91.
 20. Dahl, J. E., Liu, S. G., & Carlson, R. M. K. (2003). Isolation and structure of higher diamondoids, nanometer-sized diamond molecules. *Science*, *299*(5603), 96-99.
 21. Nguyen, T. X., & Philp, R. P. (2016). Separation of diamondoids in crude oils using molecular sieving techniques to allow compound-specific isotope analysis. *Organic Geochemistry*, *95*, 1-12.
 22. He, M., Moldowan, J. M., Nemchenko-Rovenskaya, A., & Peters, K. E. (2012). Oil families and their inferred source rocks in the Barents Sea and northern Timan-Pechora Basin, Russia. *AAPG bulletin*, *96*(6), 1121-1146.
 23. Huang, L., Zhang, S., Wang, H., Fu, X., Zhang, W., Xu, Y., & Wei, C. (2011). A novel method for isolation of diamondoids from crude oils for compound-specific isotope analysis. *Organic Geochemistry*, *42*(5), 566-571.
 24. Jimenez-Cruz, F., & García-Gutiérrez, J. L. (2020). Molecular size and shape properties of diamondoid molecules occurring in crude oil. *Arabian Journal of Chemistry*, *13*(12), 8592-8599.
 25. LAMMPS Molecular Dynamics Simulator. (n.d.). LAMMPS Molecular Dynamics Simulator. <https://www.lammps.org/#gsc.tab=0>

-
26. VMD - Visual Molecular Dynamics. (n.d.). VMD - Visual Molecular Dynamics. <https://www.ks.uiuc.edu/Research/vmd/>
 27. LeSar, R. (2013). Introduction to computational materials science: fundamentals to applications. *Cambridge University Press*.
 28. Frenkel, D., & Smit, B. (2001). Understanding molecular simulation: from algorithms to applications (Vol. 1). *Elsevier*.
 29. Haile, J. M. (1992). Molecular dynamics simulation: elementary methods. *John Wiley & Sons, Inc.*
 30. Nguyen, T. X., Cohaut, N., Bae, J. S., & Bhatia, S. K. (2008). New method for atomistic modeling of the microstructure of activated carbons using hybrid reverse Monte Carlo simulation. *Langmuir*, *24*(15), 7912-7922.
 31. Nguyen, T. X., & Bhatia, S. K. (2011). How water adsorbs in hydrophobic nanospaces. *The Journal of Physical Chemistry C*, *115*(33), 16606-16612.
 32. Database of Zeolite Structures. (n.d.). Database of Zeolite Structures. <http://www.iza-structure.org/databases/>
 33. K. Momma and F. Izumi (2011). VESTA 3 for three-dimensional visualization of crystal, volumetric and morphology data. *Appl. Crystallogr.*, *44*, 1272-1276.
 34. Nguyen, V. T., Nguyen, P. T., Dang, L. X., Mei, D., Wick, C. D., & Do, D. D. (2014). A comparative study of the adsorption of water and methanol in zeolite BEA: a molecular simulation study. *Molecular Simulation*, *40*(14), 1113-1124.
 35. Di Lella, A., Desbiens, N., Boutin, A., Demachy, I., Ungerer, P., Bellat, J. P., & Fuchs, A. H. (2006). Molecular simulation studies of water physisorption in zeolites. *Physical Chemistry Chemical Physics*, *8*(46), 5396-5406.
 36. Open Babel. (n.d.). Open Babel. https://openbabel.org/wiki/Main_Page
 37. Jorgensen, W. L., Maxwell, D. S., & Tirado-Rives, J. (1996). Development and testing of the OPLS all-atom force field on conformational energetics and properties of organic liquids. *Journal of the American Chemical Society*, *118*(45), 11225-11236.
 38. Online Cheminformatics Toolkit. (n.d.). Online Cheminformatics Toolkit. <https://mulan.pharmacy.pitt.edu>
 39. Nath, S. K., Escobedo, F. A., & de Pablo, J. J. (1998). On the simulation of vapor-liquid equilibria for alkanes. *The Journal of chemical physics*, *108*(23), 9905-9911.
 40. Nath, S. K., & de Pablo, J. J. (2000). Simulation of vapour-liquid equilibria for branched alkanes. *Molecular Physics*, *98*(4), 231-238.
 41. Nath, S. K., & Khare, R. (2001). New forcefield parameters for branched hydrocarbons. *The Journal of Chemical Physics*, *115*(23), 10837-10844.
 42. Jorgensen, W. L., & Severance, D. L. (1990). Aromatic-aromatic interactions: free energy profiles for the benzene dimer in water, chloroform, and liquid benzene. *Journal of the American Chemical Society*, *112*(12), 4768-4774.

-
43. Chitra, R., & Yashonath, S. (1997). Estimation of error in the diffusion coefficient from molecular dynamics simulations. *The Journal of Physical Chemistry B*, 101(27), 5437-5445.
 44. Ford, D.C., Dubbeldam, D., Snurr, R.Q.: The effect of framework flexibility on diffusion of small molecules in the metal-organic framework IRMOF-1. *Diffusion Fundamentals III*, 459–466 (2009).
 45. Murugan, N. A., & Yashonath, S. (2005). Pressure-induced ordering in adamantane: A Monte Carlo simulation study. *The Journal of Physical Chemistry B*, 109(5), 2014-2020.
 46. Murugan, N. A., Rao, R. S., Yashonath, S., Ramasesha, S., & Godwal, B. K. (2005). High-pressure study of adamantane: Variable shape simulations up to 26 GPa. *The Journal of Physical Chemistry B*, 109(36), 17296-17303.
 47. 47. Bárcia, P. S., Silva, J. A., & Rodrigues, A. E. (2005). Adsorption equilibrium and kinetics of branched hexane isomers in pellets of BETA zeolite. *Microporous and mesoporous materials*, 79(1-3), 145-163.
 48. King, E. M., Gebbie, M. A., & Melosh, N. A. (2019). Impact of rigidity on molecular self-assembly. *Langmuir*, 35(48), 16062-16069.

Mean square displacement

There is a combination of Fick's law with an equation that expresses the conservation of the total amount of material to compute the time evolution of the concentration profile:

$$\frac{\partial c(r, t)}{\partial t} + \nabla \cdot j(r, t) = 0 \quad (\text{A.1})$$

Combining the equation of Einstein's relation (2.15) and Fick's first law (2.16), we obtain

$$\frac{\partial c(r, t)}{\partial t} - D(\nabla^2 c(r, t)) = 0 \quad (\text{A.2})$$

Vietnamese-German University

With the boundary condition:

$$c(r, 0) = \delta(r) \quad (\text{A.3})$$

($\delta(r)$ is the Dirac delta function) to yield

$$c(r, t) = \frac{1}{(4\pi Dt)^{\frac{d}{2}}} \exp\left(-\frac{r^2}{4Dt}\right) \quad (\text{A.4})$$

where d denotes the dimensionality of the system (usually $d = 3$). The mean square displacement over the molecules have moved in time t $\langle r^2(t) \rangle$ can be obtained by multiplying equation (A.2) by r^2 and integrating over all space with the assumption

$$\int dr, c(r, t) = 1 \quad (\text{A.5})$$

This yields

$$\frac{\partial}{\partial t} \int drr^2 c(r, t) = D \int drr^2 \nabla^2 c(r, t) \quad (\text{A.6})$$

After the partial integration to the right-hand side, Einstein's relation is obtained

$$\frac{\partial \langle r^2(t) \rangle}{\partial t} = 2D \quad (\text{A.7})$$

Velocity autocorrelation function

For convenience, only one Cartesian component of the mean square displacement is considered, and if $r^2(t)$ is the time integral of the displacement of the tagged particle velocity

$$\langle r^2(t) \rangle = \left\langle \left(\int_0^t v_x(t') dt' \right)^2 \right\rangle \quad (\text{B.1})$$

$$= \int_0^t \int_0^t dt' dt'' \langle v_x(t') v_x(t' + \Delta t) \rangle \quad (\text{B.2})$$

$$= 2 \int_0^t \int_0^{t'} dt' dt'' \langle v_x(t') v_x(t' + \Delta t) \rangle \quad (\text{B.3})$$

Where $\langle v_x(t') v_x(t'') \rangle$ is called the velocity autocorrelation function. It is an equilibrium property and describes the correlation between the velocity of a particle at different times t' and t'' . As an equilibrium property, the VAF depends only on time t' and t'' , it can be written as follows:

$$\langle v_x(t') v_x(t'') \rangle = \langle v_x(0) v_x(t' + \Delta t) \rangle \quad (\text{B.4})$$

And there is the relation between the diffusion coefficient and the particles' velocity

$$2D = \lim_{t \rightarrow \infty} \frac{\partial \langle x^2(t) \rangle}{\partial t} \quad (\text{B.5})$$

Combining equations (B.2) and (B.3), we get

$$D = \int_0^\infty d\tau \langle v_x(\tau) v_x(0) \rangle \quad (\text{B.6})$$

where $\tau = t - t'$

Radial distribution function

The RDF is given by

$$\rho g(r) = \frac{1}{N} \left\langle \sum_{i=1}^N \sum_{j \neq i}^N \delta(\mathbf{r} - \mathbf{r}_{ij}) \right\rangle \quad (\text{C.1})$$

where N denotes the overall number of atoms, $\rho = N/V$ is the density, \mathbf{r}_{ij} is the vector from atom i to j , and time average is signified by angular bracket. The structural arrangement of atoms in substances that are homogeneous uniform is determined solely by the distance r among atoms and is unaffected by the separation direction of vector r , so equation (C.1) reduces to.

$$\rho g(r) = \frac{1}{N} \left\langle \sum_{i=1}^N \sum_{j \neq i}^N \delta(r - r_{ij}) \right\rangle \quad (\text{C.2})$$

Equation (C.2) can be rewritten as below due to double summation of the term $N(N-1)$ but only $\frac{1}{2}N(N-1)$ of those terms are unique

$$\rho g(r) = \frac{2}{N} \left\langle \sum_i^N \sum_{j < i}^N \delta[r - r_{ij}] \right\rangle \quad (\text{C.3})$$

The normalization of RDF can be yielded by integration of all available separation between two atoms

$$\rho \int g(r) dr = \frac{2}{N} \left\langle \sum_{i=1}^N \sum_{j < i}^N \int \delta(r - r_{ij}) dr \right\rangle \quad (\text{C.4})$$

After alternatively applying integration, summation, and changing the order of time average with the normalization condition of δ as below

$$\int \delta(r - r_{ij}) dr = 1 \quad (\text{C.5})$$

Equation (C.4) reduces to

$$\rho \int_0^\infty g(r) dr = \frac{2}{N} \left\langle \sum_{i=1}^N \sum_{j < i}^N \int_0^r \delta(r - r_{ij}) dr \right\rangle = N - 1 \approx N \quad (\text{C.6})$$

Equation (C.6) indicates that there are $(N - 1)$ other atoms in the system around each determined atom and is the foundation of interpreting $g(r)$ probabilistically

$$\rho g(r) = \frac{1}{N - 1} \left\langle \sum_{i=1}^N \sum_{j \neq i}^N V(r_{ij}, \Delta r) \right\rangle \quad (\text{C.7})$$

where $V(r, \Delta r) = \Delta r$ denotes the spherical shell volume.

In order to achieve the formula for $g(r)$ from simulation data, equation (C.3) is rewritten by applying small but finite shell thickness Δr .


$$\rho \sum_{\Delta r} g(r) V(r, \Delta r) = \frac{2}{N} \sum_{\Delta r} \left\langle \sum_{i=1}^N \sum_{j < i}^N \int \delta[r - r_{ij}] \Delta r \right\rangle \quad (\text{C.8})$$

A counting operation is represented by the double sum on the right-hand side (rhs) of equation (C.6)

$$\sum_{i=1}^N \sum_{j < i}^N \int \delta(r - r_{ij}) \Delta r = N(r, \Delta r) \quad (\text{C.9})$$

where $N(r, \Delta r)$ is the number of atoms located in a spherical shell with radius r and thickness Δr , with the shell centered on another atom. Putting equation (C.9) into (C.8) yields:

$$g(r) = \frac{\langle N(r, \Delta r) \rangle}{\frac{1}{2} N \rho V(r, \Delta r)} \quad (\text{C.10})$$


Vietnamese-German University

Explicitly expressing the time average across a total of M time steps provides

$$g(r) = \frac{\sum_{k=1}^M N_k(r, \Delta r)}{M \left(\frac{1}{2} N \right) \rho V(r, \Delta r)} \quad (\text{C.11})$$

The value chosen for the shell thickness Δr is an adjustment: it must be limited to resolve essential aspects of $g(r)$, but yet large enough to offer an appreciative sampling population for statistically credible results. Levels at $\Delta r = 0.025\sigma$ balance these competing elements satisfactorily.